united nations
educational, scientific
and cultural
organization

international atomic
energy agency

the
abdus salam
international centre for theoretical physics

SMR 1521/17

AUTUMN COLLEGE ON PLASMA PHYSICS

13 October - 7 November 2003

Hydrodynamic Instabilities in Laser Produced Plasmas

S. Atzeni

Universita' "La Sapienza" and INFM
Roma, Italy

UNIVERSITA' DEGLI STUDI DI ROMA
LA SAPIENZA
DIPARTIMENTO DI ENERGETICA

Hydrodynamic Instabilities in Laser Produced Plasmas

Stefano Atzeni

Dipartimento di Energetica
Università di Roma "La Sapienza" and INFM
Via A. Scarpa, 14-16, 00161 Roma, Italy
E-mail: atzeni@uniroma1.it

Autumn College on Plasma Physics
The Abdus Salam International Centre for Theoretical Physics
Trieste, 13 October – 7 November 2003

The following material is Chapter 8 of the book

"Physics of inertial confinement fusion"

by

S. Atzeni and J. Meyer-ter-Vehn

Clarendon Press, Oxford

(to appear in Spring 2004)

DRAFT

for personal use,
but NOT FOR CITATION

8

HYDRODYNAMIC STABILITY

This chapter is devoted to hydrodynamic instabilities. ICF capsule implosions are inherently unstable. In particular, the Rayleigh-Taylor instability (RTI) tends to destroy the imploding shell (see Fig. 8.1). It should be clear that the goal of central hot spot ignition depends most critically on how to control the instability. This is a major challenge facing ICF.

Fig. 8.1

For this reason, large efforts have been undertaken over the last two decades to study all aspects of RTI and related instabilities. Significant progress has been made, based on theory, simulations, and experiments. They show impressive agreement. Of course, the ultimate experiment will be the first successful ignition of an ICF capsule, and this is still ahead.

In an attempt to cover most of these recent results, the present chapter has become longer than others and contains many more references and a bibliographical note. Together with Chapter 12 on fast ignition, it may also be among the first that need update in a future edition of this book. Here, starting from basic theory, we develop the linear theory in much detail, including most importantly

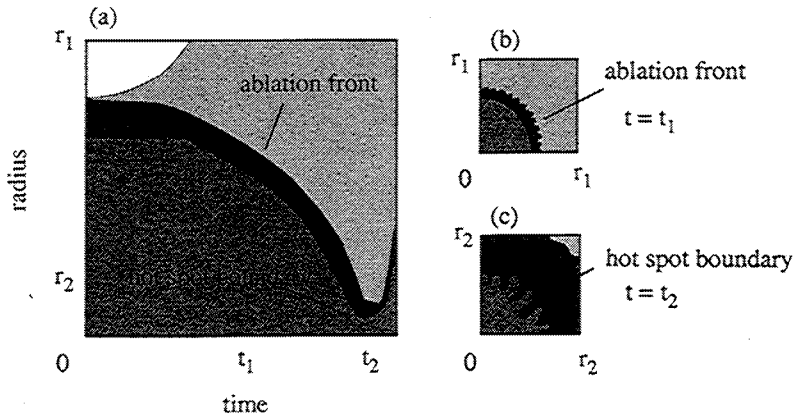

FIG. 8.1. Rayleigh-Taylor instabilities occur at two stages of the implosion of an ICF shell. The outer surface of the shell is unstable when the shell is accelerated inward by the pressure exerted by the beam-heated plasma. The inner shell surface becomes unstable when the shell is slowed down by the hot spot gas.

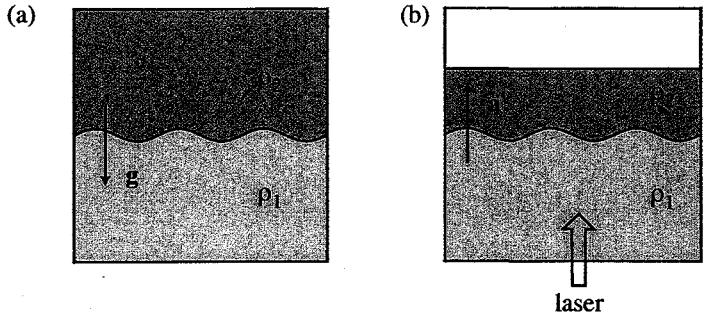

FIG. 8.2. Rayleigh-Taylor instability of (a) superimposed fluids and (b) an accelerated fluid layer. The two cases are equivalent. In both cases instability occurs because exchanging the position of elements of equal volume of fluids 1 and 2 (with $\rho_1 < \rho_2$) reduces the potential energy.

the stabilizing effects of ablative RTI, and apply it to actual ICF implosions, deriving the admissible levels of non-uniformity in capsule make and implosion drive. We also describe the nonlinear growth of bubbles and spikes, including turbulent mixing.

It is worth observing that RTI and RMI play an important role in many complex phenomena, such as some stages of stellar evolution, fragmentation of vapour films, deceleration of laser generated plumes, underground salt domes, and volcanic islands; see Dimonte (1999) and references therein. Currently, laser-driven experiments on RTI and RMI are being performed as scaled-down test-beds of models of astrophysical phenomena (Remington *et al.* 1999).

8.1 Fluid instabilities and ICF: a preview

8.1.1 *Rayleigh-Taylor instability, RTI*

The basic mechanisms of the RTI can be illustrated by referring to the simple configuration of Fig. 8.2(a), showing a vessel containing two immiscible fluids of different densities separated by a plane, horizontal boundary at $z = 0$. The fluids are subjected to gravity, $\mathbf{g}$, and fluid 1 with density ρ_1 supports fluid 2 with density ρ_2. The fluids are in hydrostatic equilibrium for any value of the density ratio ρ_2/ρ_1. However, when the upper fluid is heavier than the lower one ($\rho_2 > \rho_1$), the small perturbations of the interface rapidly grow in time. Soon spikes of the heavier fluid fall down, while bubbles of the lighter fluid rise. The instability, first studied by Lord Rayleigh in 1883, occurs because any exchange of position between two elements with equal volume of the two fluids leads to a decrease of the potential energy of the system. The same considerations can be applied in a straightforward manner to the interface between two fluids in an accelerated frame [see Fig. 8.2(b)]. This is for instance the case of an ICF shell driven by hot ablating plasma. In a frame moving with the interface the fluid effectively sees an inertial force per unit mass $\mathbf{g} = -\mathbf{a}$, where $\mathbf{a}$ is the

Fig. 8.2

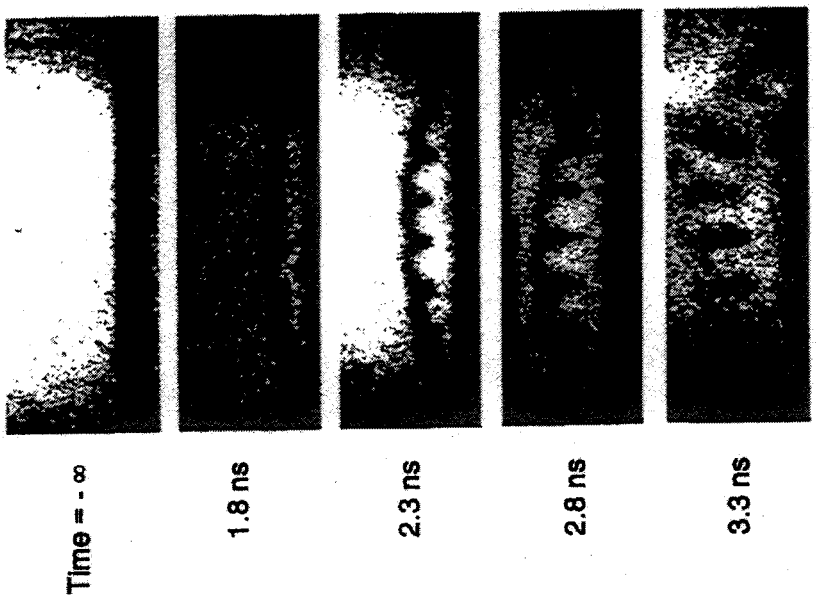

FIG. 8.3. Rayleigh-Taylor instability of a laser accelerated plane target. The target, which appears as a black area in the pictures, is irradiated by a laser beam on the right hand side. Reprinted from Nakai *et al.* (1995), with permission.

acceleration. The interface is then unstable if the acceleration is directed towards the denser fluid, which is just the case of the outer surface of an ICF shell during the stage of inward acceleration. The first theoretical analysis and experimental results on the instability of an accelerated layer were published by Taylor (1950) and Lewis (1950), respectively. In the current literature, the instability of both accelerated fluids and fluids in a gravitational field are referred to as Rayleigh-Taylor instability.

Fig. 8.3

A beautiful example of RTI of an accelerated layer is shown in Fig. 8.3 [after Nakai *et al.* (1995)]. It refers to a laser-accelerated 25 μm thick plastic foil, with an imposed initial sinusoidal corrugation of amplitude of 1.5 μm and wavelength of 100 μm. The foil is irradiated by a pulse of green laser light (wavelength $\lambda = 0.53$ μm) of intensity $I = 2 \times 10^{14}$ W/cm^2. Laser induced ablative pressure drives the foil with an acceleration of $a \simeq 10^{16}$ cm/s^2. The picture, obtained by optical diagnostics, shows the amplification of the perturbations up to a point where the foil integrity is lost. One should not be worried by the large amplitude of the perturbation, which results from the relatively large imposed corrugation.

Linear theory (see § 8.2) shows that sinusoidal perturbations of the unstable interface with wavelength λ and initial amplitude $\zeta_0 \ll \lambda$ grow exponentially in time, according to $\zeta = \zeta_0 \exp(\sigma_{RT} t)$, with linear growth rate

$$\sigma_{RT} = \sqrt{2\pi A_t a/\lambda} = \sqrt{A_t a k}, \tag{8.1}$$

where $k = 2\pi/\lambda$ is the wavenumber of the perturbation and

$$A_t = \frac{\rho_2 - \rho_1}{\rho_2 + \rho_1} \tag{8.2}$$

is the Atwood number of the interface. According to eqn 8.1 the growth rate diverges as the wavelength ~~lambda~~ $\lambda \to 0$. Actually, for very short wavelengths one should take into account surface tension and viscosity, which reduce instability growth. However, as we shall see in § 8.2.5 and § 8.2.6, both these effects turn out to be negligible in ICF.

~~does not apply for very short wavelengths, which are stabilized by viscosity. For typical ICF parameters, however, this only occurs for $\lambda \leq 1$ μm, and is of little practical relevance~~.

As the perturbation amplitude ζ becomes comparable to the wavelength (say, as $\zeta \simeq \lambda/2\pi$), the pace of growth slows down. This phenomenon is called *linear growth saturation*. At this stage an initially sinusoidal perturbation becomes asymmetric. At a fluid-vacuum interface one observes [see Fig. 8.4(a)] a large curvature bubble asymptotically rising at constant velocity and a fluid spike falling down at constant acceleration. In the case of a boundary separating two fluids of different densities, the falling spike is slowed down and deformed by the Kelvin-Helmoltz instability, and mushroom-like patterns develop [see Fig. 8.4(b)]. Asymptotically, mushroom-headed spikes fall at constant velocity. Fig. 8.4

Perturbations of real surfaces are not sinusoidal, but can anyhow be thought of as the sum of a large number of sinusoidal modes. In this case, in the nonlinear stage the various modes interact with each other and a nearly turbulent regime occurs (see Fig. 8.5). Experiments show that the penetration of bubbles of the lighter fluid into the denser fluid is well described by the law $h_b = \alpha a t^2$, with $\alpha = 0.05$–0.07. Here t is the time after the onset of turbulent behaviour. Fig. 8.5

8.1.2 *RTI and ICF*

Equation 8.1 refers to the *classical RTI* of incompressible fluids, and neglects such effects as density gradients, thermal conduction and ablation. A simple estimate shows that, unless these processes reduce the RTI growth rate well below the classical value, ICF by spherical shell implosion would fail. Following Bodner (1991), we consider a single mode perturbation and take a wavelength $\lambda = 3\Delta R$, where ΔR is the in-flight shell thickness. We take this wavelength as the most dangerous mode for shell integrity, since it evolves linearly up to an amplitude $\zeta \approx \lambda/2\pi \simeq \Delta R/2$, which would threaten the integrity of the

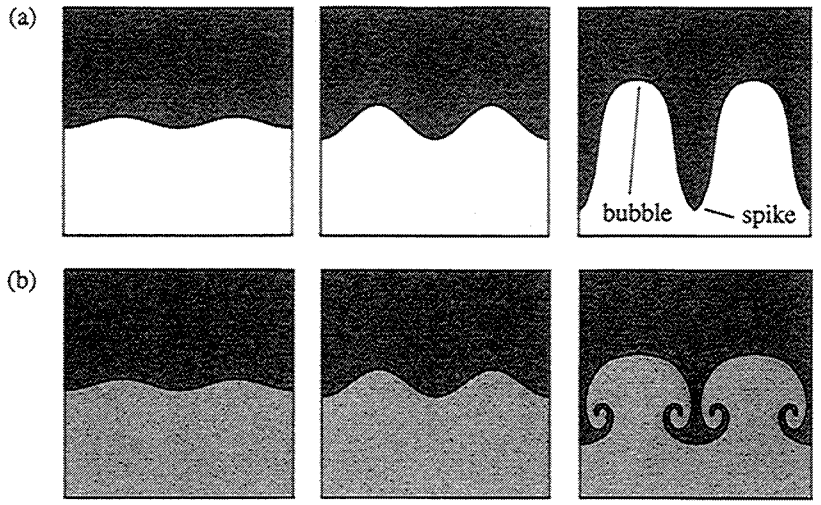

FIG. 8.4. Non linear evolution of a single-wavelength Rayeigh-Taylor instability. a) Instabiliity of a fluid-vacuum interface ($A_t = 1$); b) instability of the interface between fluids of different densities ($A_t < 1$).

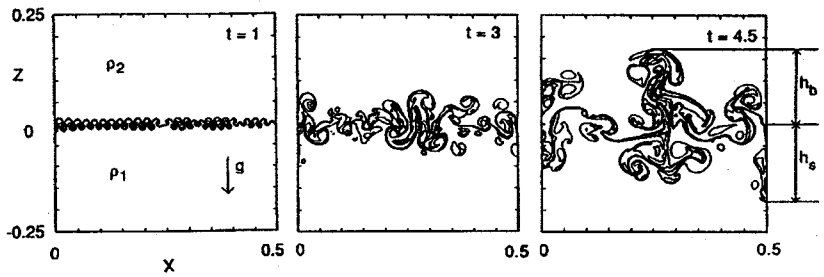

FIG. 8.5. Turbulent mixing resulting from the nonlinear evolution of a multi-wavelength RTI of superposed fluids with density ratio $\rho_2/\rho_1 = 2$. After Atzeni and Guerrieri (1993).

shell. Longer wavelengths grow slowlier, while shorter wavelengths saturate at smaller amplitudes. We assume that the ICF shell, with initial radius R_0, is imploded half way to $R = R_0/2$ at constant acceleration a, which takes a time $t_0 = \sqrt{R_0/a}$. At this time, a perturbation with initial amplitude ζ_0 would then reach an amplitude $\zeta = \zeta_0 \exp(\sigma_{RT} t_0) = \zeta_0 \exp\sqrt{2R_0/\Delta R}$. Since typical ICF shells have $R_0/\Delta R > 40$, then net perturbation growth would be about 8000. In order to keep the final perturbation amplitude smaller than $\Delta R/2 \approx 10$–20 μm, initial perturbations should be at the level of 1-2 nm. This is below practical

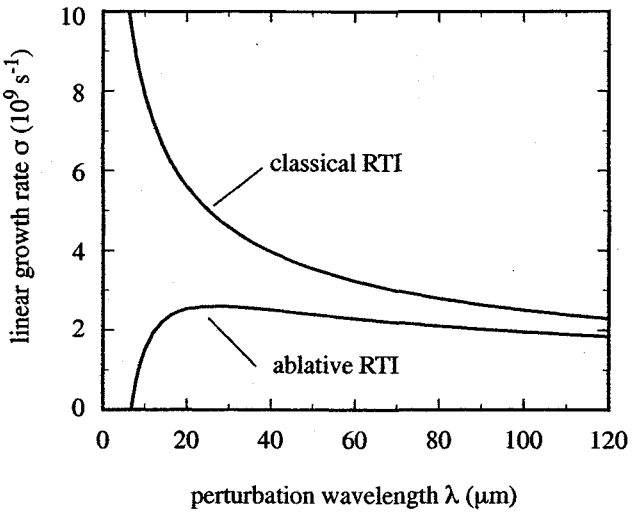

FIG. 8.6. Growth rate vs wavelength for classical RTI and for ablative RTI. Both curves are computed for the same acceleration $a = 10^{16}$ g/cm^2. The ablative case (eqn 8.3) assumes $u_a = 5 \times 10^5$ cm/s, $L = 1$ μm and $\beta = 1.5$.

limits.

Fortunately, ablation effects reduce linear growth substantially. Theory and numerical simulations indeed show that the linear growth rate of the RTI of an ablation front is well approximated by

$$\sigma = \sqrt{\frac{ak}{1+kL}} - \beta k u_a, \tag{8.3}$$

where L is a characteristic density scalelength at the ablation front, β is coefficient in the range 1–3, and u_a is the ablation velocity, i.e. the velocity of penetration of the ablation front through the dense matter (see § 8.4). Equation 8.3, which is also represented in Fig. 8.6 for parameters typical of indirect-drive ICF, shows that the finite density gradient reduces the growth rate and that ablation even stabilizes perturbations of short wavelengths. As we shall see in § 8.4.5, data from highly sophisticated recent experiments are in qualitative agreement with eqn 8.3. RTI at an ablation front will be discussed in some detail in § 8.4. Many features not taken into account in the classical RTI treatment will also be discussed at appropriate places in § 8.2–§ 8.5. Fig. 8.6

The above discussion clearly shows that even perturbations described by linear theory can pose a serious threat to ICF. For this reason, in this chapter we discuss linear evolution in detail. Concerning nonlinear aspects, we introduce the basic ideas and show some results of general interest, often without presenting detailed derivations. The interested reader can refer to the literature quoted in the individual sections and in the bibliographical section.

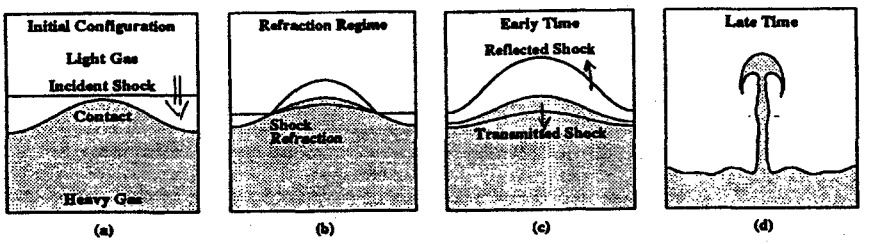

FIG. 8.7. Richtmyer-Meshkov instability. It is caused by a downward moving shock wave crossing the deformed interface between fluids of different density. After Grove *et al.* (1993), reprinted with permission.

8.1.3 *Richtmyer-Meshkov instability, RMI*

A process related to RTI was predicted by Richtmyer (1960) and was demonstrated experimentally by Meshkov (1969). It is now known as Richtmyer-Meshkov instability (RMI). It occurs when a shock wave crosses the interface between two different fluids which is not perfectly flat; see Fig. 8.7. In this case, the passage of the shock suddenly distorts the boundary and imparts to it a nonuniform velocity, causing amplification of the perturbation. RMI is important in ICF because it can produce seeds which are later amplified by the more violent RTI.

Fig. 8.7

8.1.4 *Kelvin-Helmoltz instability, KHI*

The Kelvin-Helmoltz instability (KHI) concerns the equilibrium of a stratified fluid, when the different layers are in shear motion. The simplest case is that of two superimposed thick fluid layers moving with opposite velocities (see Fig. 8.8). Small sinusoidal perturbations of the interface grow exponentially in time. As the perturbation amplitude becomes comparable to the wavelength, the perturbed interface becomes asymmetric and characteristic *rolls* appear; see Fig. 8.8(b). KHI occurs frequently in nature. For instance, it is responsible for the excitation of waves by winf on sea water, and for the oscillating structures observed at the boundaries of the wake of a ship. In ICF, KHI plays some role in the nonlinear evolution of RTI bubbles, where it produces mushroom-shaped structures, and in the interaction between neighbouring RTI bubbles. A qualitative description

Fig. 8.8

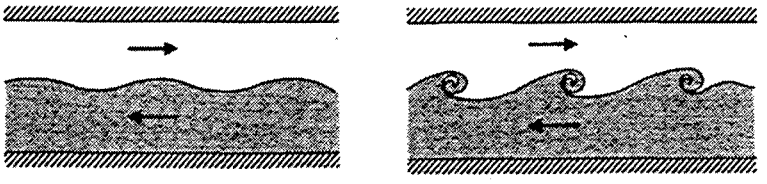

FIG. 8.8. Kelvin-Helmoltz instability. Adapted after Acheson (1990), with permission.

of the KHI mechanism will be given later in § 8.2.7.

8.2 Stability of plane interfaces

The fundamental question to be answered when dealing with the stability of a fluid equilibrium is the response to small perturbations. This is addressed by linear stability analysis, which applies to perturbations of small amplitude. They can be considered as the superposition of independently evolving sinusoidal *modes* $A(t)\sin kx$, characterized by wave number $k = 2\pi/\lambda$ and wavelength λ and with amplitudes varying like $A(t) \sim \exp(\sigma t)$. The main objective of linear theory is to determine the *dispersion relation*

$$\sigma = \sigma(k),$$

relating the linear growth rate σ to the wavenumber.

In this section, we apply linear stability theory to the potential flow model of an incompressible fluid. We first present a simple derivation of the dispersion relations of the RTI, the KHI and the RMI of plane boundaries separating homogeneous and incompressible fluids. Then, we study the RTI of accelerated foils and surfaces accelerated by a nonuniform pressure, two topics of great relevance to ICF. The presentation closely follows the treatment by Kull (1991). The potential flow model will be used again in § 8.5 to study the stability of spherical boundaries.

8.2.1 *Potential flow equations for incompressible fluids*

Simple, instructive and rather general linear solutions are obtained by using the potential flow model of an incompressible fluid subjected to gravity. One starts from the assumption of irrotational motion, $\nabla \times \mathbf{u} \equiv 0$, which allows us to write the fluid velocity as the gradient of a potential, i.e.

$$\mathbf{u} = \nabla\varphi. \tag{8.4}$$

We recall that irrotationality implies conservation of circulation, provided the fluid motion is isentropic, i.e. adiabatic and with constant entropy throughout the fluid. In such a case, a flow being everywhere irrotational at some initial time, will remain irrotational. Potential flow is a good approximation to the actual fluid motion when dissipation is negligible and when the flow is not hindered by solid bodies immersed in the fluid. A discussion can be found in textbooks on hydrodynamics (e.g. Landau and Lifshitz 1987, § 9).

We also assume that the fluid is incompressible, which is appropriate if both the fluid velocity and the phase velocity of relevant perturbations are small compared with that of sound (see Landau and Lifshitz 1987, §10). By expressing the velocity through eqn 8.4, the incompressibility condition $\nabla \cdot \mathbf{u} = 0$ becomes

$$\nabla^2\varphi = 0, \tag{8.5}$$

i.e. the Laplace equation for the potential φ.

We now need an equation for the evolution of the flow. We start by writing Newton's law along particle trajectories:

$$\rho\left(\frac{\partial \mathbf{u}}{\partial t}+\mathbf{u}\cdot\nabla\mathbf{u}\right)=-\nabla p+\mathbf{F}, \tag{8.6}$$

where $\mathbf{F}=\rho\mathbf{g}$ is the force of gravity per unit volume of fluid. We choose a reference system oriented in such a way that gravity is directed along the negative z-axis, $\mathbf{g}=-g\mathbf{e_z}$, where g is a positive quantity, and introduce a gravitational potential U, such that $\mathbf{F}=-\rho\nabla U$. Inserting this last equation and eqn 8.4 for the velocity into eqn 8.6, we get

$$\rho\nabla\left(\frac{\partial\varphi}{\partial t}+\frac{u^2}{2}+U\right)+\nabla p=0, \tag{8.7}$$

which can be integrated to obtain

$$\frac{\partial\varphi}{\partial t}+\frac{u^2}{2}+gz+\frac{p}{\rho}=C(t). \tag{8.8}$$

This is one of the forms of Bernoulli's equation. Here $C(t)$ is an arbitrary time-dependent gauge function. A useful gauge when dealing with an interface at uniform pressure $p=p_0$ is $C(t)=p_0/\rho$, from which we get

$$\frac{\partial\varphi}{\partial t}+\frac{u^2}{2}+gz=0. \tag{8.9}$$

In ICF, the effect of gravity is negligible, but the fluid is accelerated and flow perturbations are best studied in a non-inertial frame moving with the fluid interface. When the acceleration (relative to an inertial frame) is $\mathbf{a}=a\mathbf{e}_z$, where $\mathbf{e}_z$ is the unit vector parallel to the x-axis, Bernoulli's equation takes just the same form as eqn 8.9, with g replaced by a, and with φ, u and z measured in the accelerated frame.

In the following we shall focus on the case of accelerated systems, which is of primary importance to ICF, and therefore use the symbol a for acceleration throughout. However, it should be understood that all results also apply to the gravitational case when replacing a with g. In any case, equations will be written in the reference frame comoving with the boundary.

8.2.2 *Fluid boundaries*

The next step concerns the conditions to be satisfied at a fluid boundary, in particular at the surface separating two homogeneous fluid regions, for which both the Laplace equation for the potential and the Bernoulli equation apply. The surface moves with the fluid, therefore the normal components of the fluid velocities on both sides of the surface have to be continuous. Let the coordinates of the points on the surface be $\mathbf{x}(t)$, which obey the equation $S(\mathbf{x},t)=0$. The

equation for the velocity components is found as follows. Since the surface moves with the fluid the total time derivative of S must be identically zero on both sides of the interface. Introducing explicitly the dependence on space and time, $S(\mathbf{x}, t)$ must satisfy

$$\frac{DS}{dt} = \frac{\partial S}{\partial t} + \mathbf{u} \cdot \nabla S = 0, \tag{8.10}$$

on both sides of the interface. Writing the interface equation in the form $z = \zeta(x, y, t)$, then $S \equiv z - \zeta$. This is particularly convenient when considering a nearly flat, nearly horizontal surface. The interface equation 8.10 can then be written as

$$(\partial_t \zeta + u_x \partial_x \zeta + u_y \partial_y \zeta - u_z)_{z=\zeta^\pm} = 0, \tag{8.11}$$

which has to be evaluated on both sides of the interface, formally denoted by $z = \zeta^+$ and $z = \zeta^-$, and hence represents two equations. Equation 8.11 is often referred to as the *kinematic interface condition.*

A *dynamical interface condition* is obtained by considering the forces acting on the interface. At equilibrium the pressures on the opposite sides of the interface differ by an amount depending on the surface tension $\mathcal{T}$ and on the curvature of the boundary. Using square brackets to denote the *jump* of a quantity through the interface ($[f] := f_+ - f_-$), we have

$$[p] = \mathcal{T}\left(\frac{1}{R_\mathrm{a}} + \frac{1}{R_\mathrm{b}}\right) = \mathcal{T}\left(\partial^2_{xx}\zeta + \partial^2_{yy}\zeta\right), \tag{8.12}$$

where R_a and R_b are the principal radii of curvature of the surface at the considered point. They have to be taken as positive when the centre of curvature lies on the upper side of the interface (where the upper position is defined with reference to downward directed gravity or upward directed acceleration). In cases with $\mathcal{T} \simeq 0$ (typical for ICF applications), one has $[p] = 0$.

Using Bernoulli's equation 8.9 to express the pressure on both sides of the interface, eqn 8.12 becomes

$$\left[\rho\left(\partial_t \varphi + u^2/2 + az\right)\right] = \mathcal{T}\left(\partial^2_{xx}\zeta + \partial^2_{yy}\zeta\right). \tag{8.13}$$

For a fluid - vacuum interface and $\mathcal{T} = 0$ eqns 8.11 and 8.13 simplify to:

$$(\partial_t \zeta + u_x \partial_x \zeta + u_y \partial_y \zeta - u_z)_{z=\zeta} = 0\,, \tag{8.14}$$

$$\left(\partial_t \varphi + u^2/2 + az\right)_{z=\zeta} = 0\,. \tag{8.15}$$

8.2.3 *Small perturbations: linearized equations*

We now study the evolution of small perturbations of a hydrostatic equilibrium. For simplicity, from now on we consider superimposed fluids with a horizontal unperturbed interface $z(x, y) = 0$. The equation of the perturbed interface can therefore be expressed as $z = \zeta(x, y, t)$. We recall that the analysis applies either to downward directed gravity $\mathbf{g} = -a\mathbf{e}_z$ or upward directed acceleration $\mathbf{a} = a\mathbf{e}_z$.

In general, any flow quantity will be written as

$$F(x,y,z,t) = F_0(z) + \tilde{F}(x,y,z,t),$$

where the index 0 refers to unperturbed quantities, and the tilde to the perturbed quantities, coming with index 1 below the interface and 2 above. At equilibrium the vertical component of the velocity vanishes everywhere. Concerning the horizontal component, we take $u_y = 0$ everywhere and a uniform (but otherwise arbitrary) velocity for each fluid in the x direction, i.e. $u_x = u_{x1}$, for $z < 0$, and $u_x = u_{x2}$, for $z > 0$. With this notation, the velocity of fluid 1 is $\mathbf{u}_1 = (u_{x0_1} + \tilde{u}_{x_1})\mathbf{e}_x + \tilde{u}_y\mathbf{e}_y + \tilde{u}_z\mathbf{e}_z$.

Perturbed quantities have to satisfy the kinematic and dynamic boundary conditions (eqns 8.11 and 8.13, respectively), just as the equilibrium quantities. Assuming that all perturbations have small amplitudes, we linearize the relevant equations, i.e. neglect second order terms, such as products of perturbed quantities.

The linearized kinematic interface conditions 8.11 then become

$$\partial_t\zeta + u_{x0_1}\partial_x\zeta - \partial_z\tilde{\varphi}_1 = 0\,, \tag{8.16}$$

$$\partial_t\zeta + u_{x0_2}\partial_x\zeta - \partial_z\tilde{\varphi}_2 = 0\,, \tag{8.17}$$

while the dynamic condition 8.13 reads

$$\begin{aligned}\rho_1(\partial_t\tilde{\varphi}_1 + u_{x0_1}\partial_x\tilde{\varphi}_1) - \rho_2(\partial_t\tilde{\varphi}_2 + u_{x0_2}\partial_x\tilde{\varphi}_2)\\ +a\zeta(\rho_1 - \rho_2) - \mathcal{T}(\partial^2_{xx} + \partial^2_{yy})\zeta = 0,\end{aligned} \tag{8.18}$$

where we have used $\tilde{u}_z = \partial_z\tilde{\varphi}$ and have neglected second order terms such as $\tilde{u}_x\partial_x\zeta$. Equations 8.16–8.18 have to be evaluated at the unperturbed interface position $z = 0$.

8.2.4 *Normal mode analysis and dispersion relation*

The assumption of small perturbations allows us to use the superposition principle, i.e. to describe the perturbed fluid motion as the sum of linearly independent *modes*. Here we consider a plane interface, while the case of spherical geometry will be addressed in § 8.5. We then take sinusoidal modes and seek for solutions in which any perturbed quantity $\tilde{F}$ evolves in time proportionally to $\mathrm{e}^{\sigma t}$:

$$\tilde{F} \propto \cos(k_x x + k_y y)\mathrm{e}^{\sigma t}.$$

Formally, this can be done by performing a Fourier transformation of the relevant equations both in the x and y coordinates and in time, i.e. by performing the replacement

$$\tilde{F}(x,z,t) \to \Re\left[\hat{\tilde{F}}(k_x,k_y,z)\mathrm{e}^{i(k_x x + k_y y - \omega t)}\right], \tag{8.19}$$

where the real numbers k_x and k_y are the components of the wavevector, $\hat{\tilde{F}}$ is a complex amplitude, and ω is a complex frequency. The great advantage of such

an approach is that derivatives with respect to t, x and y can be replaced by products

$$\frac{\partial}{\partial t} = -i\omega, \tag{8.20}$$

$$\frac{\partial}{\partial x} = ik_x, \tag{8.21}$$

$$\frac{\partial}{\partial y} = ik_y. \tag{8.22}$$

In the following, all equations are understood as written for the amplitudes $\hat{\tilde{F}}$ and only the real part of each quantity is taken; for simplicity of notation the circumflex and the $\Re$ sign will be omitted.

It is useful to write the frequency by separating the real and the imaginary parts, i.e.,

$$\omega = \omega_{\mathrm{R}} + i\sigma, \tag{8.23}$$

where $\omega_{\mathrm{R}} = \Re(\omega)$ and $\sigma = \Im(\omega)$. Perturbed quantities will then evolve proportionally to

$$\Re(\mathrm{e}^{ik_x x}\mathrm{e}^{ik_y y}\mathrm{e}^{-i\omega_{\mathrm{R}} t})\mathrm{e}^{\sigma t} = \cos(k_x x + k_y y - \omega_{\mathrm{R}} t)\mathrm{e}^{\sigma t}. \tag{8.24}$$

A mode with given wavevector $\mathbf{k} = k_x \mathbf{e}_x + k_y \mathbf{e}_y$ will grow indefinitely, if the *linear growth rate* $\sigma = \sigma(\mathbf{k})$ is positive. *Instability will occur if* $\sigma(\mathbf{k}) > 0$ *for at least one* $\mathbf{k}$. Notice that a positive linear growth rate corresponds to *exponential growth* of the amplitude of the relevant mode. Linear stability analysis aims at determining the spatial shape $\tilde{F}(\mathbf{k}, z)$ of the allowed perturbation modes, the *dispersion relation* $\omega = \omega(\mathbf{k})$, and hence the relationship $\sigma = \sigma(\mathbf{k})$ between the linear growth rate and the perturbation wavevector.

We start by analyzing the spatial distribution of the perturbation. From the Fourier transform of the Laplace equation (8.5), we find that the perturbed potential satisfies

$$\left(-k_x^2 - k_y^2 + \partial_{zz}^2\right)\tilde{\varphi}(z) = 0, \tag{8.25}$$

which has the general solution

$$\tilde{\varphi}(z) = A\mathrm{e}^{kz} + B\mathrm{e}^{-kz}\,, \tag{8.26}$$

where we have set $k^2 = k_x^2 + k_y^2$. Since the perturbations must vanish as $z \to \pm\infty$ and $\tilde{u}_z$ has to be continuous at $z = 0$, one has

$$\tilde{\varphi}(z) = \begin{cases} \tilde{\varphi}_1(z) = A\mathrm{e}^{kz} & \text{for } z \leq 0, \\ \tilde{\varphi}_2(z) = -A\mathrm{e}^{-kz} & \text{for } z \geq 0, \end{cases} \tag{8.27}$$

with $A = \tilde{u}_z(z = 0)/k$. Perturbations therefore peak on the interface and decay exponentially with scale-length $1/k = \lambda/2\pi$.

Next, we study the time evolution. From the Fourier transform of eqns 8.16 and 8.17 we get

$$-i(\omega - k_x u_{x0_1})\zeta - \partial_z \tilde{\varphi}_1 = 0, \tag{8.28}$$
$$-i(\omega - k_x u_{x0_2})\zeta - \partial_z \tilde{\varphi}_2 = 0, \tag{8.29}$$

and substituting eqn 8.27 for the spatial part of the potentials we have

$$-i(\omega - k_x u_{x0_1})\zeta - Ak = 0, \tag{8.30}$$
$$-i(\omega - k_x u_{x0_2})\zeta + Ak = 0. \tag{8.31}$$

Analogously, from the Fourier transform of eqn 8.18 and eqn 8.27 we obtain

$$-i(\omega - k_x u_{x0_2})\rho_2 A/\zeta - i(\omega - k_x u_{x0_1})\rho_1 A/\zeta - (\rho_2 - \rho_1)a + k^2\mathcal{T} = 0. \tag{8.32}$$

The desired dispersion relation is then found by eliminating A/ζ in the first two terms through eqns 8.30 and 8.31, respectively, which gives

$$(\omega - k_x u_{x0_2})^2\rho_2 + (\omega - k_x u_{x0_1})^2\rho_1 = -[(\rho_2 - \rho_1)a - k^2\mathcal{T}]k. \tag{8.33}$$

Solving for $\omega = \omega(k)$, we get the general dispersion relation

$$\omega = k_x \overline{u}_{x0} \pm i\sqrt{\frac{(\rho_2 - \rho_1)a - k^2\mathcal{T}}{\rho_1 + \rho_2}k + k_x^2\rho_1\rho_2\left[\frac{u_{x0_1} - u_{x0_2}}{\rho_1 + \rho_2}\right]^2}, \tag{8.34}$$

where $\overline{u}_{x0} = (\rho_1 u_{x0_1} + \rho_2 u_{x0_2})/(\rho_1 + \rho_2)$. Obviously, it is convenient to refer to a frame moving with velocity $\mathbf{u} = \overline{u}_{x0}\mathbf{e}_x$, so that the first term on the right-hand side of eqn 8.34 vanishes. We now consider particular cases of eqn 8.34 to obtain the linear growth rates for the Rayleigh-Taylor and Kelvin-Helmholtz instabilities.

8.2.5 *Classical RTI growth rate*

Classical RTI refers to superimposed fluids with no tangential velocity shear, i.e. $u_{x0_1} = u_{x0_2}$. From eqn 8.34 and the definition of σ in eqn 8.23 we then have

$$\sigma = \sqrt{\frac{(\rho_2 - \rho_1)ak - k^3\mathcal{T}}{\rho_1 + \rho_2}}. \tag{8.35}$$

When the argument of the square root is positive, the growth rate is real and positive, leading to exponential growth of the perturbation. In the opposite case, σ is imaginary and corresponds to undamped oscillations, known as internal gravity waves. Equation 8.35 shows that the interface is stable if $\rho_2 < \rho_1$, i.e. if the denser liquid supports the lighter one. In the opposite case surface tension stabilizes modes with wavelength $\lambda < 2\pi\mathcal{T}/[(\rho_2 - \rho_1)a]$, but longer wavelengths grow unboundedly, and therefore the system is unstable. In ICF and in many

other applications, however, the effect of surface tension is negligible. E.g., in ICF implosions, one has $a > 10^{15}$ cm/s^2, and even taking for $\mathcal{T}$ the very high value $\mathcal{T} = 500$ g/(cm s^2) referring to a mercury-water interface, only wavelengths smaller than about 10^{-7} cm are stabilized. Neglecting surface tension, one gets the *classical Rayleigh-Taylor growth rate*:

$$\sigma = \sigma_{RT} = \sqrt{A_t a k}, \tag{8.36}$$

where $A_t = (\rho_2 - \rho_1)/)(\rho_2 + \rho_1)$ is the *Atwood number*. It is useful to notice that the linear growth rate only depends on the absolute value of the wavenumber $k = |\mathbf{k}|$, not on its components k_x and k_y. This means, e.g., that the linear growth of disturbances with $k = k_x$ and $k_y = 0$ is just the same as that of disturbances with the same value of $k = (k_x^2 + k_y^2)^{1/2}$.

8.2.6 *Influence of viscosity and compressibility on RTI*

In the previous derivation of the classical RTI growth rate we did not take into account viscosity and compressibility. Here, we show that in ICF the effect of viscosity is indeed always negligible, while that of compressibility is marginal.

Concerning viscosity, Menikoff *et al.* (1977) have shown that the growth rate of the RTI of superimposed viscous fluids is well approximated by

$$\sigma = (A_t a k)^{1/2} \left[(1 + w)^{1/2} - w)^{1/2} \right], \tag{8.37}$$

where $w = \frac{\overline{\nu}_k^2 k^3}{A_t a}$, $\overline{\nu}_k = (\mu_1 \rho_1 + \mu_2 \rho_2)/(\rho_1 + \rho_2)$ is a density averaged kinematic viscosity, and μ_1 and μ_2 are the viscosities of the two fluids. For small values of w, eqn yields the classical inviscid result, while in the opposite limit $\sigma \simeq A_t a \lambda / 4\pi \overline{\nu}_k$, showing that the growth rate vanishes as $\lambda/\overline{\nu}_k \to 0$. It is also easily found that the growth rate is maximum for $\lambda = \lambda_m = 4\pi(\overline{\nu}_k^2/A_t a)^{1/3}$. For application to ICF, we can use the expression for the viscosity of a fully ionized plasma (Spitzer 1962)

$$\mu = 2.21 \times 10^{-15} \frac{T_i^{5/2} A^{1/2}}{Z^4 \ln \Lambda} \text{ g/(cm s)}, \tag{8.38}$$

where T_i is the ion temperature in Kelvin, A and Z are the atomic mass and charge, respectively, and $\ln \Lambda$ is the Coulomb logarithm. Application of eqn 8.37 to the ablation front of an ICF target is not straightforward because density and temperature vary sustantially in space. However, one can estimate $\overline{\nu}$ as the ratio of the viscosity of the hot plasma close to the ablation front to the density of the dense shell. It then turns out that viscosity can only reduce the growth of modes with wavelengths smaller than a fraction of a micron. It is instead ineffective on the modes with wavelengths of 10–60 μm, which are the most dangerous for the integrity of shells with in-flight thickness $\Delta R \approx 5$–20 μm.

Regarding compressibility, Bernstein and Book (1983) have shown that the growth rate of the instability of plane interfaces with $A_t = 1$ is unaffected by compressibility, whatever the adiabatic index γ of the fluid. This result is relevant

to the instability at the ablation front, where the Atwood number is close to unity. For different values of A_t, compressibility results in growth rates higher than the classical one, but the effect is small as far as $a/kc_2^2 \ll 1$, $c_2 = (\gamma p/\rho_2)^{1/2}$ being the sound speed in the denser fluid. For an accelerated shell of thickness ΔR, one has $a \simeq p/\rho\Delta R$ so that the previous condition becomes $k\Delta R \gg 1/\gamma$, or $\lambda \ll 2\pi\gamma\Delta R$, which is marginally satisfied for the most dangerous modes for target integrity. More details on the effect of compressibility on the ablative RTI can be found in a paper by Piriz (2001b). At implosion stagnation the effect of compressibility is not negligible, but still not so large as to alter qualitatively the picture of the instability (see § 8.5.3).

8.2.7 *KHI growth rate*

The growth rate of the KHI is obtained from eqn 8.34 by considering fluids of equal density, no acceleration, i.e. $a = 0$, and with a given tangential velocity discontinuity ($u_{x01} \neq u_{x02}$). In the frame moving with $u_x = (u_{x0_1} + u_{x0_2})/2$ and neglecting surface tension, we have

$$\sigma = \sigma_{\mathrm{KH}} = k_x|u_{x0_1} - u_{x0_2}|, \tag{8.39}$$

showing that surface perturbations with wavevector parallel to the fluid velocity grow exponentially, with rate proportional to the velocity difference. For obvious symmetry reason the rate σ is independent of the sign of such a velocity difference. Perturbations with wavevector orthogonal to the unperturbed velocity, instead, are unaffected. The effects of gravity and surface tension on KHI are discussed e.g. in the textbooks by Chandrasekhar (1961) and Acheson (1990).

We can now give a simple explanation of the mechanism of KHI. Let us consider a small disturbance of the horizontal surface separating two counterstreaming fluids; see Fig. 8.9. According to Bernoulli's equation 8.8, in steady state the sum $(u^2/2)+p/\rho$ is constant along each horizontal streamline. It follows that the fluid pressure is lower (higher) where the velocity is higher (lower). Therefore the pressure increases in regions such as those labelled "a" in the figure, where the flow tube widens and decreases in regions "b" where the flow tube shrinks. Such a pressure imbalance enhances the initial surface deformation, resulting in instability.

Fig. 8.9

8.2.8 *Time evolution*

According to the previous discussion, unstable RTI and KHI modes grow exponentially in time. However, the initial surface perturbations do not necessarily coincide with pure modes, which have initial amplitude and velocity related by $\zeta_0 = \dot{\zeta}_0/\sigma$. Here, we study how a general single wavelength perturbation evolves in time. A case of particular interest is that of static initial perturbations with $\dot{\zeta}_0 = 0$. The results of this section will be exploited later, in the analysis of the RTI of a fluid layer of finite thickness (§ 8.2.9), the Richtmyer-Meshkov instability (§ 8.2.10), and the response to transient perturbations (§ 8.2.11).

From now on we restrict ourselves to two-dimensional perturbations, i.e. consider an x,y slab geometry with the flow independent of the y coordinate. We

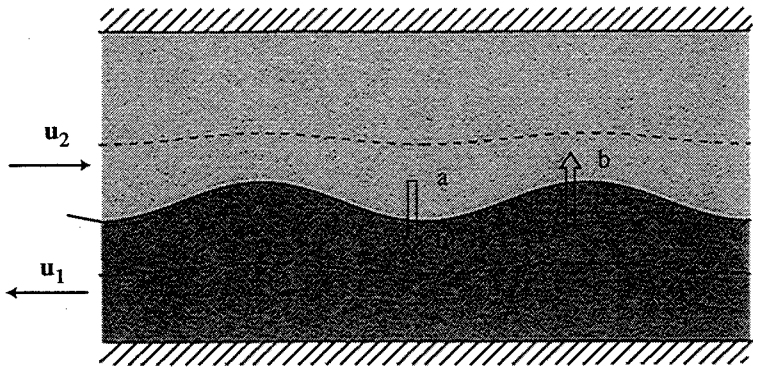

FIG. 8.9. Mechanism of KHI growth. Pressure imbalance due to surface deformation positively feedbacks to the deformation, causing instability.

also set $u_{x0} = 0$, but allow for time dependent acceleration $a(t)$. Performing Fourier transform in x of eqns 8.11 and 8.13, we obtain

$$\partial_t \zeta + k\tilde{\varphi}_2 = 0, \tag{8.40}$$

$$\partial_t \zeta - k\tilde{\varphi}_1 = 0, \tag{8.41}$$

$$-[\rho(\partial_t \tilde{\varphi} + a(t)\zeta)]_2 + [\rho(\partial_t \tilde{\varphi} + a(t)\zeta)]_1 = -\mathcal{T}k^2\zeta. \tag{8.42}$$

Next, we differentiate eqns 8.40 and 8.41 with respect to time, solve for the perturbed potential, and insert the result into eqn 8.42, thus obtaining a second order ordinary differential equation for the time evolution of the amplitude ζ:

$$\partial_{tt}^2 \zeta - \left(A_t a k - \frac{k^3 \mathcal{T}}{\rho_1 + \rho_2} \right) \zeta = 0. \tag{8.43}$$

If acceleration a is constant, we have

$$\partial_{tt}^2 \zeta - \sigma^2 \zeta = 0, \tag{8.44}$$

where $\sigma(k)$ is time independent and given by eqn 8.35. By solving eqn 8.44 with initial conditions $\zeta(t=0) = \zeta_0$ and $\zeta(t=0) = \dot{\zeta}_0$, we find that the amplitude of a sinusoidal perturbation with mode number k, initial amplitude ζ_0 and initial velocity $\dot{\zeta}_0$ evolves in time according to

$$\zeta(t) = \zeta_0 \cosh(\sigma t) + \frac{\dot{\zeta}_0}{\sigma} \sinh(\sigma t). \tag{8.45}$$

Notice that the growth is purely exponential only if $\zeta_0 = \dot{\zeta}_0/\sigma$, corresponding to the evolution of an eigenfunction of RTI. Equation 8.45 can be used to test the

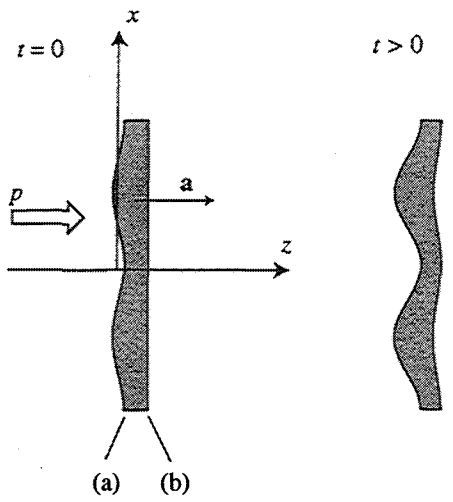

FIG. 8.10. RTI of a fluid layer, accelerated by a pressure p applied on the left-hand side.

accuracy of numerical codes. For sufficiently large time, such that $\sigma t \gg 1$, we have exponential growth:

$$\zeta(t) \approx \frac{\zeta_0 + \dot{\zeta}_0/\sigma}{2} e^{\sigma t}, \tag{8.46}$$

with growth rate σ and effective initial amplitude $\zeta_{\text{eff}} = (\zeta_0 + \dot{\zeta}_0/\sigma)/2$.

8.2.9 *RTI layers of finite thickness and feedthrough*

So far we have dealt with semi-infinite fluids, but, in fact, in ICF we want to accelerate relatively thin shells. The stability of a fluid layer accelerated by uniform pressure applied to one of its surfaces is discussed in this section, following Taylor's original presentation (1950).

We refer to a fluid layer of thickness Δz delimited by the boundaries (a) at $z = 0$ and (b) $z = \Delta z$; a pressure is applied on surface (a), causing constant acceleration $a > 0$ (see Fig. 8.10). As usual, we assume 2D sinusoidal perturbations $z = \zeta(x,t) = \hat{\zeta}(t)\cos(kx)$ with wavenumber $k = 2\pi/\lambda$ and omit the circumflex, so that ζ, $\tilde{\varphi}$, etc refer to the amplitude of the perturbed quantities. According to the discussion for semi-infinite fluids, we expect that surface (a), where the acceleration is directed from vacuum to fluid is unstable, while surface (b) is stable. We shall soon see that this is qualitatively correct, but that perturbations also grow at (b).

Fig. 8.10

We assume static initial perturbations at both surfaces,

$$\zeta_a(t = 0) = \zeta_{a0}, \tag{8.47}$$

$$\zeta_b(t=0) = \zeta_{b0}, \tag{8.48}$$

$$\dot{\zeta}_a(t=0) = \dot{\zeta}_b(t=0) = 0. \tag{8.49}$$

Following the results of §8.2.4, we write the potential perturbation as

$$\tilde{\varphi}(z,t) = \tilde{\varphi}_a(t)e^{-kz} + \tilde{\varphi}_b(t)e^{-k(\Delta z - z)}. \tag{8.50}$$

In order to get the equations for the evolution of $\tilde{\varphi}_a(t)$ and $\tilde{\varphi}_b(t)$, we write the kinematic and dynamic interface conditions at both surfaces of the layer. We then differentiate the dynamical equations and substitute $\partial_t \zeta_{1,2}$ from the kinematic equations, thus getting

$$\partial_{tt}^2 \tilde{\varphi}_a(t) - ak\tilde{\varphi}_a(t) = 0, \tag{8.51}$$

$$\partial_{tt}^2 \tilde{\varphi}_b(t) + ak\tilde{\varphi}_b(t) = 0. \tag{8.52}$$

The solutions of these equations, satisfying the initial condition $u = 0$ in the whole fluid layer, are

$$\tilde{\varphi}_a(t) = \tilde{\varphi}_{a0} \sinh \sigma t\ , \tag{8.53}$$

$$\tilde{\varphi}_b(t) = \tilde{\varphi}_{b0} \sin \sigma t\ , \tag{8.54}$$

where the growth rate takes the same value $\sigma = \sqrt{gk}$ as in the case of the interface between a semi-infinite fluid and vacuum. Inserting eqns 8.53 and 8.54 into the general expression of the potential (eqn 8.50) we have:

$$\tilde{\varphi}(z,t) = \tilde{\varphi}_{a0}e^{-kz} \sinh \sigma t + \tilde{\varphi}_{b0}e^{-k(\Delta z - z)} \sin \sigma t. \tag{8.55}$$

We see that the first term in eqn 8.55 is maximum at surface (a), and grows exponentially. The second term, instead oscillates, and is maximum at surface (b).

We are now ready to compute the time evolution at the two surfaces of the layer. Using $\zeta = \int u dt = \int \partial_z \tilde{\varphi} dt$, and imposing the initial conditions 8.47 and 8.48 we get:

$$\zeta_a(t) = \frac{\zeta_{a0} - \zeta_{b0}e^{-k\Delta z}}{1 - e^{-2k\Delta z}} \cosh \sigma t + \frac{\zeta_{b0} - \zeta_{a0}e^{-k\Delta z}}{1 - e^{-2k\Delta z}} e^{-k\Delta z} \cos \sigma t, \tag{8.56}$$

$$\zeta_b(t) = \frac{\zeta_{a0} - \zeta_{b0}e^{-k\Delta z}}{1 - e^{-2k\Delta z}} e^{-k\Delta z} \cosh \sigma t + \frac{\zeta_{b0} - \zeta_{a0}e^{-k\Delta z}}{1 - e^{-2k\Delta z}} \cos \sigma t, \tag{8.57}$$

and for sufficiently large t, such that the hyperbolic functions dominate over the circular functions:

$$\zeta_a(t) = \frac{\zeta_{a0} - \zeta_{b0}e^{-k\Delta z}}{1 - e^{-2k\Delta z}} \cosh \sigma t, \tag{8.58}$$

$$\zeta_b(t) = \zeta_a e^{-k\Delta z}. \tag{8.59}$$

Equation 8.58 shows that the perturbation of surface (a) grows as the unstable interface between a semi-infinite fluid and vacuum, but with the front factor also

depending on the initial perturbations at the opposite side of the foil and on the dimensionless foil thickness $k\Delta z$. At surface (b), the perturbation grows at the same rate as at (a), but with the amplitude reduced by a factor $\exp(-k\Delta z)$. Such a phenomenon of transmission of a perturbation from an unstable surface to a stable one is known as *feed-through* and is important for ICF. Perturbations grown at the unstable ablation front are fed to the inner surface of the solid DT fuel during inward acceleration, where they seed the instability occurring at implosion stagnation. Feed-through is, however, negligible for perturbations with wavelength much smaller than the thickness of the shell.

8.2.10 *RMI growth rate*

The classical RTI refers to constant acceleration, while impulsive acceleration can induce the Richtmyer-Meshkov instability (RMI), which is also of interest to ICF. For instance, just at the beginning of the irradiation of an ICF target, a shock wave is launched through the shell and causes sudden time-dependent acceleration. The simplest treatment of RMI is provided by the so-called impulsive model (Richtmyer 1960), which solves eqn 8.43 in the limiting case $a(t) = \Delta u \delta(t)$, where $\delta(t)$ is the delta function and Δu is the velocity increment caused by the transit of the shock at time $t = 0$. Neglecting surface tension and assuming an initial sinusoidal perturbation of wavenumber k and amplitude ζ_0, integration of eqn 8.43 gives

$$\partial_t \zeta - \zeta_0 A_t k \Delta u = 0 \tag{8.60}$$

and, integrating once again,

$$\zeta(t) = \zeta_0(1 + \sigma_{\mathrm{RM}} t); \qquad \sigma_{\mathrm{RM}} = A_t k \Delta u \,. \tag{8.61}$$

Here, the Atwood number A_t refers to the value taken just after the transit of the shock. Equation 8.61 shows that the perturbation amplitude varies linearly in time; this is easily explained by the observation that, once the shock has crossed the interface, the mechanism driving the instability ceases and one only observes an inertial evolution. Contrary to RTI, RMI occurs for any value of the Atwood number, that is both for a shock propagating from a light material to a denser one or vice versa. If $A_t < 0$, i.e. when the shock propagates from the denser material to the lighter one, the instability reverts the sign of the perturbation amplitude. Despite its apparent simplicity, the use of eqn 8.61 is not straightforward, since there is no precise rule to define the initial perturbation amplitude ζ_0. For $A_t > 0$ Richtmyer chose ζ_0 equal to the amplitude immediately after shock transit. For $A_t < 0$, Meyer and Blewett (1972) have shown that better results are obtained by using for ζ_0 the average value of the pre- and post-shock perturbation amplitudes. This is issue is discussed in the review paper by Holmes *et al.* (1999).

Experiments and numerical simulations confirm that small perturbations grow linearly in time. However, the theoretical growth rates agree with experiments and simulations only for a limited range of values of the shock strength and of the density ratio. Here, compressibility plays an important role and cannot be neglected. At present, the field is actively investigated, just to clarify

these issues. The reader is referred to the quoted paper by by Holmes *et al.*, which also includes extensive reference to alternative theoretical approaches to RMI, and compares analytical results with experiments and simulations. As far as ICF is concerned, RMI is certainly less dangerous than RTI. It grows linearly in time, while RTI grows exponentially in time. However, RMI can be important in generating seeds which are amplified by RTI later on.

8.2.11 *Nonuniform acceleration*

Laser and particle beams driving fusion capsules are not perfectly uniform and generate spatially nonuniform driving pressures and hence nonuniform acceleration. The effects on the evolution of an unstable interface can be analyzed by a simple extension of the model used so far.

Let us consider an initially flat interface driven by a pressure which causes the nonuniform acceleration $a_0 + \tilde{a}(t)\cos kx$. The amplitude of the perturbation $\zeta = \zeta(t)$ is governed by

$$\partial_{tt}^2 \zeta - \sigma^2 \zeta = \tilde{a}, \tag{8.62}$$

with $\sigma = (A_t a_0 k)^{1/2}$. This is eqn 8.43 with $\mathcal{T} = 0$ and $\tilde{a}$ describing the acceleration perturbation. The general solution of the inhomogeneous equation 8.62 is given by

$$\zeta(t) = \frac{\tilde{a}}{2\sigma}\left[e^{\sigma t}\int_0^t \tilde{a}e^{-\sigma t}dt - e^{-\sigma t}\int_0^t \tilde{a}e^{\sigma t}dt\right]. \tag{8.63}$$

Two cases are of particular interest to ICF. The first one concerns the effect of time-independent pressure nonuniformities, as they might be produced by asymmetries in the irradiation pattern. In this case eqn 8.63 becomes

$$\zeta(t) = (\tilde{a}/\sigma^2)\left[\cosh(\sigma t) - 1\right]. \tag{8.64}$$

For long enough time such that $\sigma t \gg 1$, one has $\zeta \simeq (\tilde{a}/\sigma^2)\cosh(\sigma t)$. Comparison with eqn 8.45 shows that the effect of the nonuniform acceleration is equivalent to that of an initial surface perturbation with amplitude $\zeta_0 = \tilde{a}/\sigma^2 = \tilde{a}/A_t a_0 k$.

A second situation relevant to ICF is that in which the pressure nonuniformity only occurs for a short time interval Δt, e.g. at the beginning of irradiation. In this case, $\Delta t \ll 1/\sigma$, we can approximate the perturbed acceleration by an impulsive function $\tilde{a} = \Delta u_0 \delta(t)$, and eqn 8.63 becomes

$$\zeta = (\Delta u_0/\sigma)\sinh(\sigma t). \tag{8.65}$$

Comparison with eqn 8.45 shows that the impulsive acceleration is equivalent to an initial velocity perturbation $\dot{\zeta}_0 = \Delta u_0$.

In conclusion, eqns 8.64 and 8.65 allow us to take into account pressure nonuniformities by neglecting the perturbed acceleration $\tilde{a}$ on the right-hand side of eqn 8.62 and simply introducing instead suitable initial conditions in the corresponding homogeneous equation.

8.3 RTI in fluids with arbitrary density profile

In many important cases, including ICF targets and exploding supernovas, RTI does not involve sharp interfaces between homogeneous fluids, but fluid equilibria with the density gradually changing in the direction parallel to acceleration. Here, we follow the presentation of Chandrasekhar (1961) and consider fluids in which the density may change in space, still keeping the condition of incompressibility. This allows us to study the stability of stratified fluids and to get a rather general condition for instability. In the next section, when studying the stability of an ablation layer we shall further improve the model, with the assumption of isobaricity replacing that of incompressibility.

Considering again 2D x,z perturbations and taking gravity in the negative z direction, $\mathbf{g} = -a\mathbf{e}_z$, the relevant conservation equations can be written as

$$\frac{\partial \rho}{\partial t} + \nabla \cdot (\rho \mathbf{u}) = 0, \tag{8.66}$$

$$\rho \frac{\partial u_x}{\partial t} + \rho \left(u_x \frac{\partial u_x}{\partial x} + u_z \frac{\partial u_x}{\partial z} \right) = -\frac{\partial p}{\partial x}, \tag{8.67}$$

$$\rho \frac{\partial u_z}{\partial t} + \rho \left(u_x \frac{\partial u_z}{\partial x} + u_z \frac{\partial u_z}{\partial z} \right) = -\frac{\partial p}{\partial z} - \rho a, \tag{8.68}$$

$$\frac{\partial u_x}{\partial x} + \frac{\partial u_z}{\partial z} = 0. \tag{8.69}$$

8.3.1 *Linearized perturbation equations*

Assuming small perturbations around an equilibrium characterized by $u_{x0} = u_{z0} = 0$, $\rho(z, t = 0) = \rho_0(z)$, and using the tilde to denote perturbations, eqns 8.66 – 8.69 become

$$\frac{\partial \tilde{\rho}}{\partial t} + \tilde{u}_z \frac{d\rho_0}{dz} = 0, \tag{8.70}$$

$$\rho_0 \frac{\partial \tilde{u}_x}{\partial t} = -\frac{\partial \tilde{p}}{\partial x}, \tag{8.71}$$

$$\rho_0 \frac{\partial \tilde{u}_z}{\partial t} = -\frac{\partial \tilde{p}}{\partial z} - a\tilde{\rho}, \tag{8.72}$$

$$\frac{\partial \tilde{u}_x}{\partial x} + \frac{\partial \tilde{u}_z}{\partial z} = 0, \tag{8.73}$$

Fourier transform of these equations in x and t (all quantities with tilde being proportional to $e^{ikx}e^{\sigma t}$) gives

$$\sigma \tilde{\rho} = -\tilde{u}_z \frac{d\rho_0}{dz}, \tag{8.74}$$

$$\sigma \rho_0 \tilde{u}_x = -ik\tilde{p}, \tag{8.75}$$

$$\sigma \rho_0 \tilde{u}_z = -\frac{d\tilde{p}}{dz} - a\tilde{\rho}, \tag{8.76}$$

$$ik\tilde{u}_x + \frac{d\tilde{u}_z}{dz} = 0. \tag{8.77}$$

We now combine eqns 8.74–8.77 into a single equation for $\tilde{u}_z$. We first multiply eqn 8.75 by ik and use eqn 8.77 for $\tilde{u}_x$, yielding

$$k^2\tilde{p} = -\sigma\rho_0\frac{d\tilde{u}_z}{dz}. \tag{8.78}$$

We then substitute eqn 8.74 for $\tilde{\rho}$ into eqn 8.76:

$$\frac{d\tilde{p}}{dz} = -\sigma\rho_0\tilde{u}_z + \frac{a}{\sigma}\tilde{u}_z\frac{d\rho_0}{dz}. \tag{8.79}$$

Finally, by eliminating $\tilde{p}$ in eqns 8.78 and 8.79, we obtain the desired evolution equation for $\tilde{u}_z$:

$$\frac{d}{dz}\left(\rho_0\frac{d\tilde{u}_z}{dz}\right) - \rho_0 k^2\tilde{u}_z = -\frac{k^2}{\sigma^2}a\frac{d\rho_0}{dz}\tilde{u}_z. \tag{8.80}$$

Since velocity perturbations have to vanish at large distance from the interface, we look for solutions such that $\tilde{u}_z \to 0$ as $z \to \pm\infty$. An interesting result is obtained by multiplying eqn 8.80 with $\tilde{u}_z$, giving

$$-\frac{d}{dz}\left(\rho_0\tilde{u}_z\frac{d\tilde{u}_z}{dz}\right) + \rho_0\left(\frac{d\tilde{u}_z^2}{dz}\right)^2 + \rho_0 k^2\tilde{u}_z^2 = a\frac{k^2}{\sigma^2}\frac{d\rho_0}{dz}\tilde{u}_z^2, \tag{8.81}$$

which can then be integrated over z from $-\infty$ to ∞ and solved with respect to σ to yield

$$\sigma^2 = k^2\frac{\displaystyle\int_{-\infty}^{\infty} a\frac{d\rho_0}{dz}\tilde{u}_z^2 dz}{\displaystyle\int_{-\infty}^{\infty}\rho_0(z)\left[\left(\frac{d\tilde{u}_z}{dz}\right)^2 + k^2\tilde{u}_z^2\right]dz}. \tag{8.82}$$

Notice that the integral of the first term on the left-hand side of eqn 8.81 is zero since perturbations must vanish at infinity. In eqn 8.82 we have kept a under the integral to include the case of space-dependent acceleration, which will be useful later in this section. The explicit expression 8.82 for the growth rate allows us to discuss regimes of instability in qualitative terms, as we show in the next subsection.

8.3.2 *General instability condition*

According to eqn 8.82 the condition for instability, i.e. the existence of at least one value of k for which $\sigma(k)$ is real and positive, is equivalent to the existence of values of k for which the numerator of eqn 8.82 is positive (the denominator being always positive).

It is immediately seen that the system is stable if the product $a(d\rho_0/dz)$ is everywhere negative and unstable if $a(d\rho_0/dz)$ is positive in some z interval.

If $a(d\rho_0/dz)$ is anywhere positive, then modes exist which make the integral positive. Hence, a necessary and sufficient condition for instability is that in some interval of z the product $a(d\rho_0/dz) > 0$, i.e. both density gradient and acceleration have the same sign. By using eqn 8.68 to express the acceleration as $a = -(dp_0/dz)/\rho_0(z)$, we obtain a general condition for instability in the form

$$\frac{d\rho_0}{dz}\frac{dp_0}{dz} < 0. \tag{8.83}$$

It shows that RTI occurs whenever density gradient and pressure gradient have opposite sign. When density and pressure gradients are not parallel, the condition for instability is $\nabla\rho_0 \cdot \nabla p_0 < 0$. The form 8.83 is particularly useful and physically transparent in applications to ICF and to astrophysical problems.

8.3.3 *The classical RTI growth rate*

Let us now derive the classical growth rate 8.36 from the general expression 8.82. For the configuration of § 8.2 with two superimposed homogeneous fluids 1 and 2, such that $\rho_0(z) = \rho_2$ for $z > 0$ and $\rho_0(z) = \rho_1$ for $z < 0$. The condition of continuity of the velocity component normal to the unperturbed boundary is

$$\lim_{z\to 0^+} \tilde{u}_z = \lim_{z\to 0^-} \tilde{u}_z = \tilde{u}_{z0}. \tag{8.84}$$

In each of the two regions 1 and 2 the density is uniform, and one has $d\rho_0(z)/dz = 0$; eqn 8.80 then becomes, for $z \neq 0$,

$$\frac{d^2\tilde{u}_z}{dz^2} - k^2\tilde{u}_z = 0. \tag{8.85}$$

The solution satisfying the boundary conditions at infinity and the continuity conditions at the interface is

$$\tilde{u}_z = \begin{cases} \tilde{u}_{z0}e^{-kz} & z \geq 0, \\ \tilde{u}_{z0}e^{kz} & z \leq 0. \end{cases} \tag{8.86}$$

Notice that $\tilde{u}_x = (i/k)\partial_z\tilde{u}_z$, $\partial_z\tilde{u}_z$ and $\partial_z\tilde{u}_x$ are not continuous at the interface. They would have been continuous had we taken viscosity into account.

The linear growth rate is now found by inserting the velocity perturbation 8.86, the densities, and the density derivative $d\rho_0/dz = \delta(z)(\rho_2 - \rho_1)$ into the general expression 8.82. The classical growth rate 8.36 is then immediately recovered.

8.3.4 *Density gradient*

We now turn to the case of a stratified fluid, having a region with variable density $\rho(z)$ joining two homogeneous regions with different densities ρ_1 and

ρ_2, respectively. For a simple evaluation of the growth rate, following Le Levier (1955), we take the model density profile

$$\rho_0(z) = \begin{cases} \rho_1 + (\Delta\rho/2)\exp(2z/L) & z \leq 0, \\ \rho_2 - (\Delta\rho/2)\exp(-2z/L) & z \geq 0, \end{cases} \tag{8.87}$$

where $\Delta\rho = \rho_2 - \rho_1$. Using this profile in eqn 8.82 and assuming that the perturbation eigenfunctions are still well approximated by those of eqn 8.86 for the sharp interface, one finds

$$\sigma = \sqrt{\frac{A_t a k}{1 + kL}} \tag{8.88}$$

with $A_t = \Delta\rho/(\rho_2 + \rho_1)$. This reproduces the classical RTI rate in the limit of long perturbation wavelength, $kL \ll 1$. In the opposite limit of short wavelength $kL \gg 1$, it gives $\sigma = \sqrt{aA_t/L} = \sqrt{a/2L_{\min}}$, where $L_{\min} = \min[\rho_0/(d\rho_0/dz)] = L/2A_t$ is the minimum value of the density-gradient scale-length. Therefore, short wavelength modes have a growth rate independent of the wavelength and substantially smaller than in the case of the sharp interface. Equation 8.88 is an approximate result, because we have used the eigenfunction 8.86 derived for step-like profiles. Self-consistent calculations (Munro 1988) have shown that in the limit $kL \gg 1$ the growth rate is $\sigma \simeq \sqrt{a/L_{\min}}$ which is a factor $\sqrt{2}$ larger than the present estimate. For practical application in ICF target design, we may use the approximate formula (Lindl 1997)

$$\sigma = \sqrt{\frac{A_t a k}{1 + A_t k L_{\min}}}, \tag{8.89}$$

which has the correct limits for large and small k.

8.4 RTI at an ablation front

In this section we discuss RTI at a laser- or radiation-driven front. The very important result in this case is that ablation reduces the growth of RTI modes and even fully stabilizes short wavelength modes. This is predicted by rather sophisticated theory and demonstrated by difficult and elegant experiments. Before entering the detailed treatment, we give a simple argument, which makes ablative stabilization plausible. It is due to Lindl and was reported by Kilkenny *et al.* (1994). It is based on the observation that the eigenfunctions of classical RTI grow in time as $\exp(\sigma_{RT}t)$ and decay in space as $\exp(-k|z|)$, where $|z|$ is the distance from the unstable interface (see eqn 8.27). In the ablative RTI the perturbation grows by a factor $\exp(\sigma_{RT}\Delta t)$ in the time interval Δt. Due to ablation, however, the interface moves inside the dense material with an *ablation velocity* u_a. Therefore in the time interval Δt the interface penetrates to depth $\Delta z = u_a\Delta t$ inside the dense material and samples an eigenfunction which is smaller by a factor $\exp(-k\Delta z) = \exp(-ku_a\Delta t)$. Therefore, the effective growth

using $p = \rho\Gamma_B T$. We then eliminate the time derivative of the density by using the continuity equation 8.66 in the form $-\partial\rho/\partial t = \rho\nabla\cdot\mathbf{u} + \mathbf{u}\cdot\nabla\rho$, thus getting

$$\Gamma_B\rho\left(\frac{\partial T}{\partial t} + \mathbf{u}\cdot\nabla T\right) = \frac{\partial p}{\partial t} + p\nabla\cdot\mathbf{u} + \mathbf{u}\cdot\nabla p. \tag{8.93}$$

Substituting this last equation into eqn 8.91, we obtain

$$\frac{1}{\gamma-1}\left(\frac{\partial p}{\partial t} + \mathbf{u}\cdot\nabla p\right) = -\frac{\gamma}{\gamma-1}p\nabla\cdot\mathbf{u} - \nabla\cdot\mathbf{q} \tag{8.94}$$

By assuming isobaricity, we set the left-hand side to zero and take the pressure $p = p_a$ as a constant on the right-hand side; here, we use subscript "a" to refer to quantities at the ablation front. In this isobaric approximation (Kull and Anisimov 1986) the energy conservation equation reads

$$\nabla\cdot\left(\mathbf{u} + \frac{\gamma-1}{\gamma}\frac{\mathbf{q}}{p_a}\right) = 0. \tag{8.95}$$

We now relate the heat flux $\mathbf{q} = -\chi\nabla T$ to the flow variables. For the thermal conductivity we take

$$\chi = \chi_0 T^\nu, \tag{8.96}$$

which applies to both electron heat diffusion, with $\nu = 5/2$, and to radiative heat diffusion, with $\nu > 3$ (see § 7.1.2). In typical cases energy is transported simultaneously by electrons and by photons. However, it turns out that in most cases a power law 8.96 is still an acceptable approximation, be it with values of ν different from those quoted above. When radiative effects are important in direct drive targets, Betti *et al.* (1998) find that one has $\nu < 2$, contrary to naive expectations. In passing, we mention that the derivation below also applies, when the conductivity is expressed in the more general form $\chi = \chi_0 T^\nu p^{-\mu} = \chi_0 T^\nu(\rho\Gamma_B T)^{-\mu}$. Here we set $\mu = 0$. Using the isobaric approximation, we then write the thermal flux as

$$\mathbf{q} = -\chi\nabla T = \chi_a T_a \frac{\nabla\hat{\rho}}{\hat{\rho}^{\nu+2}}, \tag{8.97}$$

where T_a is the temperature and χ_a is the conductivity at the ablation front and $\hat{\rho} = \rho/\rho_a \leq 1$ is the density normalized to its value at the ablation front. Equation 8.95 can then be written in the form

$$\nabla\cdot\left(\mathbf{u} + u_a L_0 \frac{\nabla\hat{\rho}}{\hat{\rho}^{\nu+2}}\right) = 0, \tag{8.98}$$

where

$$L_0 = \frac{\gamma-1}{\gamma}\frac{\chi_a}{\rho_a u_a}\frac{1}{\Gamma_B} \tag{8.99}$$

is a characteristic scale-length.

Summarizing, in 2D slab geometry and in the isobaric approximation, the fluid equations in the accelerated frame of reference are

$$\frac{\partial \rho}{\partial t} + \nabla \cdot (\rho \mathbf{u}) = 0, \tag{8.100}$$

$$\rho \frac{\partial u_x}{\partial t} + \rho u_x \frac{\partial u_x}{\partial x} + \rho u_z \frac{\partial u_x}{\partial z} = -\frac{\partial p}{\partial x}, \tag{8.101}$$

$$\rho \frac{\partial u_z}{\partial t} + \rho u_x \frac{\partial u_z}{\partial x} + \rho u_z \frac{\partial u_z}{\partial z} = -\frac{\partial p}{\partial z} - \rho a, \tag{8.102}$$

$$\nabla \cdot \left(\mathbf{u} + u_a L_0 \frac{\nabla \hat{\rho}}{\hat{\rho}^{\nu+2}} \right) = 0. \tag{8.103}$$

Notice that we have kept terms with pressure gradients in the momentum equations 8.101 and 8.102, because there they are of the same order as the terms on the left-hand sides.

8.4.2 *Qualitative discussion in terms of the Froude number*

Important features of the ablative RTI can be discussed qualitatively, based on the analysis of the equilibrium profiles of the ablating fluid (Betti 1996). Indeed, we expect that the general condition for instability ($\nabla\rho \cdot \nabla p < 0$; see eqn 8.83) and the growth reduction due to a density gradient (see eqn 8.89) still apply to the ablative RTI. But now mass, momentum and energy flow in addition reduce the instability growth. Furthermore, we expect that RTI modes are located in the layer where the density gradient scale-length is minimum.

We start from the density profile. By integrating eqn 8.103 and using the continuity equation 8.100, involving $\rho u = \rho_a u_a$, we find that the density gradient

$$\frac{d\hat{\rho}}{dz} = \frac{\hat{\rho}^{\nu+1}}{L_0}(1 - \hat{\rho}) \tag{8.104}$$

only depends on L_0 and the exponent ν. Corresponding profiles for different values of ν are shown versus the normalized space coordinate z/L_0 in Fig. 8.12. Equation 8.104 also shows that the local scale-length is $L = L_0/\hat{\rho}^{\nu}(1-\hat{\rho})$ has a minimum value

Fig. 8.12

$$L_{\min} = L_0 \frac{(\nu+1)^{\nu+1}}{\nu^{\nu}}, \tag{8.105}$$

which is several times larger than L_0 for $\nu > 1$. Equation 8.104 cannot be solved in closed-form, but two asymptotic limits of great interest can be obtained for the overdense region and the blow-off plasma. We find

$$\hat{\rho} \simeq \begin{cases} 1 - e^{-z/L_0}, & \text{for } z \gg L_0, \\ \left(-\dfrac{L_0}{\nu z} \right)^{1/\nu}, & \text{for } z \ll -\nu L_0. \end{cases} \tag{8.106}$$

To analyse the pressure profile, we consider momentum conservation along z expressed by eqn 8.102, which at equilibrium reads

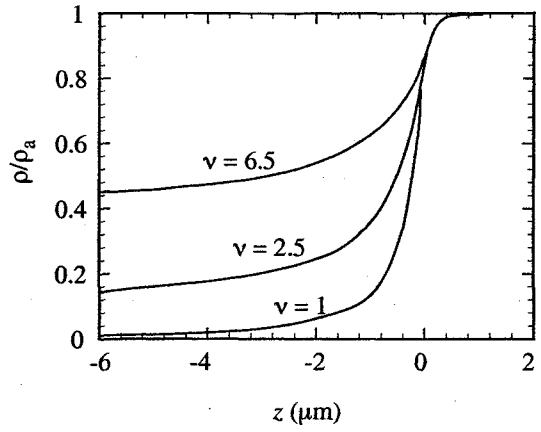

FIG. 8.12. Isobaric ablation model. Normalized density profiles around the ablation front for $L_0 = 0.1$ μm and different values of ν After Betti *et al.* (1996), with permission.

$$\rho u_z \frac{du_z}{dz} = -\frac{dp}{dz} - \rho a. \tag{8.107}$$

An expression for the velocity is found from eqn 8.100 for mass conservation in the form $u_z = u_a \rho_a / \rho = u_a / \hat{\rho}$. Here u_a is the ablation velocity, which is the velocity of the exhaust material at the ablation front measured in a frame moving with the front itself. Equation 8.107 can then be written as

$$\frac{dp}{dz} = -\rho a \left[1 - \hat{\rho}^{\nu-2}(1-\hat{\rho})\mathcal{F}\right], \tag{8.108}$$

where we have used the relationship $du_z/dz = -u_a \hat{\rho}^{-2}(d\hat{\rho}/dz)$ and eqn 8.104, and have introduced the *Froude number*

$$\mathcal{F} = \frac{u_a^2}{aL_0}. \tag{8.109}$$

The equivalent expression

$$\mathcal{F} = \frac{\rho_a u_a^3}{\chi_a T_a} \tag{8.110}$$

shows that the Froude number can be thought of as the ratio of the energy fluxes associated to hydrodynamic flow and to thermal conduction, respectively. The Froude number vanishes in the limit in which energy flux is dominated by thermal conductivity.

For qualitative stability analysis, the location of peak pressure is particularly important. It can be found by setting the pressure derivative in eqn 8.108 to zero. We thus see that peak pressure occurs at the location where the normalized density takes the value $\hat{\rho}_p$, such that $\hat{\rho}_p^{\nu-2}(1-\hat{\rho}_p)\mathcal{F} = 1$. For large Froude

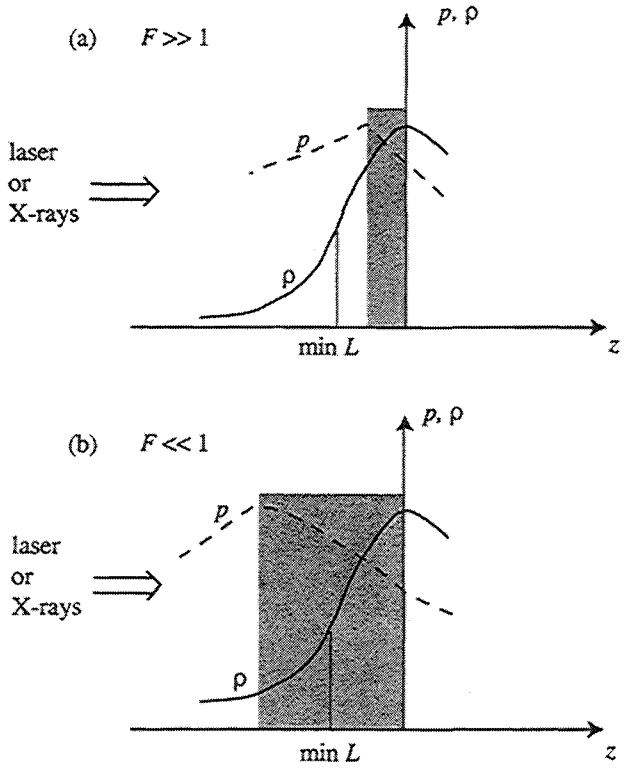

FIG. 8.13. Density and pressure profiles around the ablation front for large (a) and small (b) Froude numbers $\mathcal{F}$. RTI unstable regions (where $\nabla p \cdot \nabla \rho < 0$) are indicated by shaded areas. Short-wavelength modes, centred around the minimum of the density-gradient scale-length are unstable when they fall in the shaded area. Decreasing the Froude number makes short wavelength modes unstable. Adapted after Betti *et al.* (1996), with permission.

numbers, $\mathcal{F} \gg 1$, i.e. when thermal conductivity plays a relatively minor role, the peak pressure is found at $\hat{\rho}_p = 1 - \mathcal{F}^{-1} \simeq 1$, i.e. close to the ablation front (see Fig. 8.13a). As $\mathcal{F}$ decreases, the peak pressure moves away from the ablation front. In the limit of $\mathcal{F} \ll 1$, the pressure increases indefinitely when moving away from the ablation front.

Fig. 8.13

We have thus found that as the relative importance of the thermal conductivity increases, the peak pressure moves away from the ablation front towards the low density plasma. This widens the region of ablated plasma where $\nabla \rho \cdot \nabla p < 0$ (see Fig. 8.13b) and RTI modes are unstable. Therefore, while in principle both hydrodynamic flow and thermal conduction reduce RTI growth, this profile modification induced by thermal conduction can reduce substantially their stabilizing

effect.

We can now discuss the stability of the ablation front in terms of the Froude number. We consider first the case $\mathcal{F} \gg 1$ (see Fig. 8.13a). Since the peak pressure is close to the ablation front, the classical unstable region where $\nabla\rho \cdot \nabla p < 0$ is very small and does not include the region of steepest gradient. In addition, for large values of $\mathcal{F} = u_a^2 a/L_0 \gg 1$ we expect important stabilizing effects due to the ablative flow. All this suggests that in this case modes with wavelength comparable to or smaller than L_0 and therefore satisfying $kL_0 > 1$ are stable.

In the opposite case of $\mathcal{F} \ll 1$, a large classically unstable region exists, which now includes the region of steepest gradient (see Fig. 8.13b). In this case, ablation and density gradients cannot stabilize modes with wavelength comparable to the scale-length L_0. Indeed, stabilization is only found to occur at much shorter wavelengths.

8.4.3 *Perturbation equations*

In the following, we give the equations for the numerical stability analysis of the problem and present results in graphical form. The subsonic nature of the flow around the ablation front allows us to use the isobaric approximation for the equation describing flow perturbations (Kull and Anisimov 1986). As usual, we take perturbations proportional to $e^{ikx}e^{\sigma t}$. Linearizing eqs 8.100–8.103 around an equilibrium solution with $\mathbf{u}_0 = u_0(z)\mathbf{e}_z$, $\rho_0 = \rho_0(z)$ and $\mathbf{a}_0 = a\mathbf{e}_z$, we write in dimensionless form

$$(\hat{\rho}\sigma_n - \partial_{\hat{z}})\tilde{n} + \frac{\tilde{v}_z\hat{\rho}}{k_n\hat{L}} + \hat{\rho}\hat{\nabla}\cdot\tilde{v} = 0, \tag{8.111}$$

$$i(-\hat{\rho}\sigma_n + \partial_{\hat{z}})\tilde{v}_x + \tilde{\pi} = 0, \tag{8.112}$$

$$\partial_{\hat{z}}\tilde{\pi} - \left(\partial_{\hat{z}} - \sigma_n\hat{\rho} - \frac{1}{k_n\hat{L}}\right)\tilde{v}_z + \tilde{n}\left(\frac{\hat{\rho}}{k_n\mathcal{F}} - \frac{1}{k_n\hat{L}\hat{\rho}}\right) = 0, \tag{8.113}$$

$$\hat{\nabla}\cdot\left[\tilde{v} + k_n\hat{\nabla}\left(\frac{\tilde{n}}{\hat{\rho}^{\nu+1}}\right)\right] = 0, \tag{8.114}$$

where $\hat{z} = kz$, $\hat{\nabla} = k^{-1}\nabla$, $\hat{\rho} = \rho_0(z)/\rho_a$, $\hat{L} = L/L_0$, and $L = \hat{\rho}/(d\hat{\rho}/dz)$ are known functions of the coordinate z, $\mathcal{F} = u_a^2/aL_0$ is the Froude number introduced above,[1]

$$k_n = kL_0, \qquad \sigma_n = \sigma/ku_a \tag{8.115}$$

are dimensionless wavenumber and growth rate, respectively. Here $\tilde{n} = \tilde{\rho}/\rho$, $\tilde{v}_z = \tilde{u}_z/u_a$, $\tilde{v}_x = \tilde{u}_x/u_a$, and $\tilde{\pi} = \tilde{p}/\rho_a u_a^2$ are the four dimensionless unknowns. Equations 8.111–8.114 can be combined into a single fifth-order differential equation for $\tilde{\Phi} = k_n\tilde{n}/\hat{\rho}^{\nu+1}$:

$$[\partial_{\hat{z}}(\partial_{\hat{z}} - \sigma_n\hat{\rho})\partial_{\hat{z}} - (\partial_{\hat{z}} - \sigma_n\hat{\rho})]k_n\frac{L}{L_0}\left[(\partial_{\hat{z}} - \sigma_n\hat{\rho})\tilde{\Phi}\hat{\rho}^{\nu} + k_n\hat{\nabla}^2\tilde{\Phi}\right]$$

[1] Notice that the Froude number $\mathcal{F}$ used here is the reciprocal of the parameter Γ introduced by Kull (1989).

$$+\partial_{\hat{z}}\left(\partial_{\hat{z}}-\sigma_{\rm n}\hat{\rho}\right)\left[\partial_{\hat{z}}\tilde{\Phi}\hat{\rho}^{\nu}+k_{\rm n}\hat{\nabla}^2\tilde{\Phi}\right]+k_{\rm n}\hat{\nabla}^2\tilde{\Phi}+\frac{\tilde{\Phi}\hat{\rho}^{\nu+2}}{k_{\rm n}\mathcal{F}}=0. \quad (8.116)$$

This is an eigenvalue equation, the eigenvalue being the dimensionless growth rate

$$\sigma_{\rm n}=\sigma_{\rm n}(k_{\rm n},\mathcal{F},\nu), \quad (8.117)$$

which only depends on the dimensionless wavenumber $k_{\rm n}$ and on the parameters $\mathcal{F}$ and ν.

Equation 8.116 cannot be solved analytically to give a closed form dispersion relation. Accurate solutions have been obtained by numerical methods by Kull (1989), who extended pioneering work by Takabe *et al.* (1985). Recently, eqn 8.116 has been solved by sophisticated analytical treatments based on asymptotic matching techniques and WKB methods (Sanz 1994; Betti *et al.* 1996). Results are summarized in the next subsection.

It is also worth mentioning that many authors have developed simplified analytical treatments of the ablative RTI, based on *sharp boundary models.* Such models consider the perturbation of the interface separating two homogeneous fluids, with boundary conditions approximately taking into account mass and energy flows associated to ablation. Although less rigorous then the self-consistent theory, sharp boundary models allowed to gain understanding into ablative RTI. They were pioneered by Bodner (1974), who derived a dispersion relation ($\sigma=\sqrt{ak}-ku_{\rm a}$), showing for the first time the stabilizing effect of ablation. Recent developments of sharp boundary models of the linear ablative RTI are summarized by Piriz (2001a). Sanz *et al.* (2002) have also shown that sharp-boundary models can be also used to address nonlinear ablative RTI. They have developed a model leading to a system of two properly matched Laplace equations. Its computational solution is straightforward and fast, and allow to recover the main features of nonlinear RTI evolution.

8.4.4 *Results of self-consistent treatments*

A general dispersion relation for the ablative RTI, which fits analytical solutions of eqn 8.116 for small and large values of $\mathcal{F}$ and for the whole range of ν of practical interest has been proposed by Betti *et al.* (1998), but it is quite lengthy and is therefore not reproduced here. Results are more transparent in graphical form. In Fig. 8.14 we plot the normalized growth rate versus the normalized wavenumber for different values of Froude number and ν. It is seen that short wavelengths are stabilized, the stabilization being more effective for large values of the Froude number, in qualitative agreement with the discussion of § 8.4.2. Figure 8.14 shows the existence of a cut-off wavenumber, above which all modes are stable. The dependence of the cut-off wavenumber on the Froude number is presented in Fig. 8.15.

Fig. 8.14

Fig. 8.15

Betti *et al.* (1998) have also shown that the dispersion relation can be approximated in the form

$$\sigma=\alpha_1(\mathcal{F},\nu)\sqrt{ak}-\beta_1(\mathcal{F},\nu)ku_{\rm a} \quad \text{for } \mathcal{F}>\mathcal{F}^*(\nu), \quad (8.118)$$

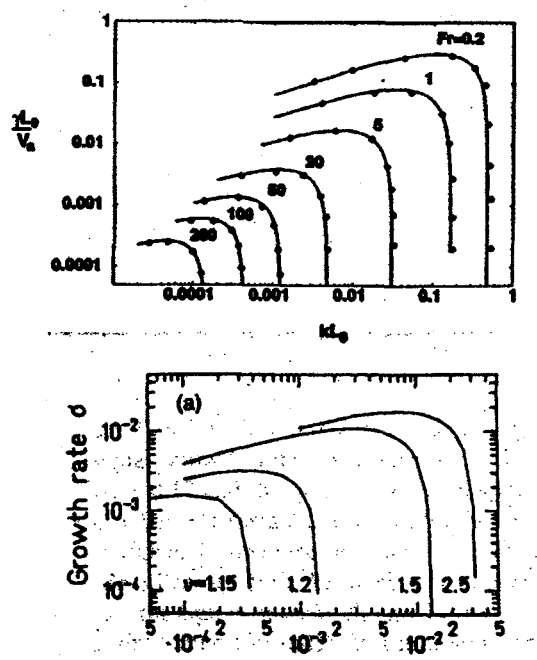

FIG. 8.14. Stability results from the isobaric ablation model with self-consistent steady-flow profiles. Instability dispersion relation $\sigma_n = \sigma_n(k_n)$ (a) for $\nu = 2.5$ with Froude number $\mathcal{F}$ varying between 0.01 and 50; (b) for $\mathcal{F} = 5$ and different values ν. Curves for $\nu > 2.5$, not shown here, almost overlap with the curve for $\nu = 2.5$. After Kull (1989), with permission.

$$\sigma = \alpha_2(\mathcal{F},\nu)\sqrt{\frac{ak}{1+kL_{\min}}} - \beta_2(\mathcal{F},\nu)ku_a \quad \text{for } \mathcal{F} \le \mathcal{F}^*(\nu), \tag{8.119}$$

where α_1, α_2, β_1 and β_2 are fitting functions depending only on $\mathcal{F}$ and ν. They are presented in graphical form in Fig. 8.16. The same figure also shows the regions of best fit of each of eqns 8.118 and 8.119. Fig. 8.16

Equations 8.118 and 8.119 are known as *Takabe's formula* and *modified Takabe's formula*, respectively. Equation 8.118, with $\beta_1 \simeq 3$, was first proposed by Takabe *et al.* (1985) to fit results of a numerical eigenvalue solution of a model of the ablative RTI assuming spherical geometry and steady coronal flow. This formula provides simple, useful expressions for the cut-off wavenumber

$$k_c = \frac{\alpha^2}{\beta^2}\frac{a}{u_a^2} = \frac{1}{L_0}\frac{\alpha^2}{\beta^2}\mathcal{F} \tag{8.120}$$

and for the maximum value of the growth rate

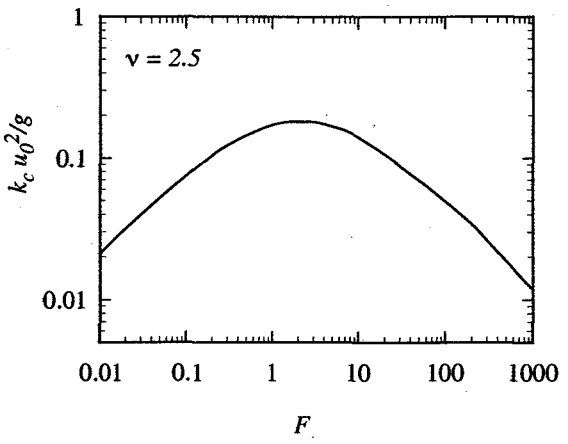

FIG. 8.15. Normalized cut-off wavelength vs Froude number $\mathcal{F}$ for conductivity exponent $\nu = 2.5$, as predicted by the isobaric model with self-consistent steady-flow profiles. After Kull (1989), with permission.

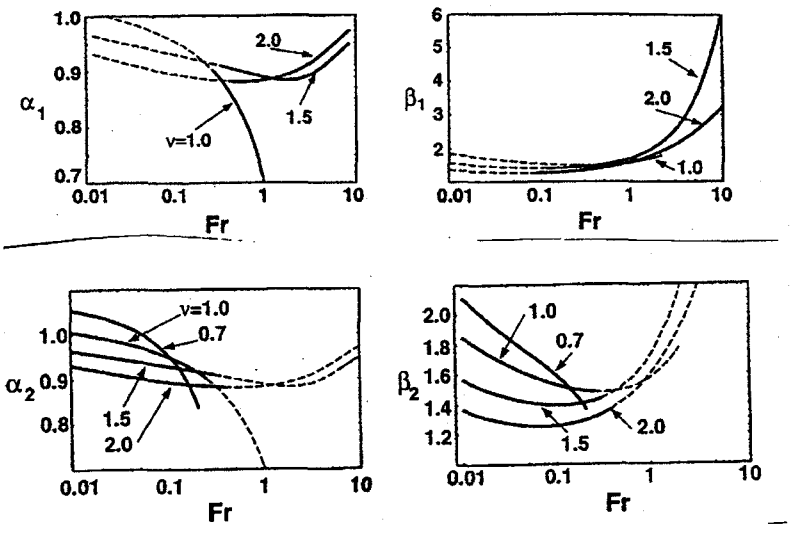

FIG. 8.16. Coefficients α_1 and β_1, and α_2 and β_2 of the fitting formulas 8.118 and 8.119 versus the Froude number $\mathcal{F}$, for different values of the effective conductivity exponent ν. The solid part of each curve indicates the region of best fit of either eqn 8.118 or 8.119. After Betti *et al.* (1998).

	direct-drive (plastic ablator)	direct-drive (DT ablator)	indirect-drive
α_1		0.97	
β_1		2.5	
α_2	0.97		1
β_2	1.5		1–1.5

Table 8.1 *Values of the coefficients α_1, α_2 η_1, and η_2 appearing in eqn 8.119, for ICF targets designed to achieve ignition.*

$$\sigma_m = \sigma(k_{\rm m}) = \frac{1}{4}\frac{\alpha^2}{\beta}\frac{a}{u_{\rm a}}, \tag{8.121}$$

which occurs at $k = k_{\rm m} = k_{\rm c}/4$. Notice that eqn 8.120 confirms the qualitative prediction made in § 8.4.2 about modes with $kL_0 \approx 1$: indeed they are stable for $\mathcal{F} \gg 1$ and unstable for $\mathcal{F} \ll 1$.

Equations 8.118 and 8.119 summarize the present understanding of the linear theory of the ablative RTI. However, their use is not straightforward. Indeed, first they require the knowledge of $\mathcal{F}$, ν, $u_{\rm a}$ and $L_{\rm min}$, while in the experiments the independent variables are the target and beam parameters. Second, the model used here is based on the assumption that energy transport can be described by a single diffusive process.

Despite these limitations, detailed comparison with 2D numerical simulations confirm the approximate validity of these results, provided the values of the relevant quantities $\mathcal{F}$, $u_{\rm a}$, a, ν $L_{\rm min}$ are properly evaluated. To this purpose, the standard procedure (Betti *et al.* 1998) consists in performing accurate 1D numerical radiation-hydrodynamic simulations, including both flux-limited electron conductivity and multi-group radiation transport, to find quasi-equilibrium profiles of the flow quantities. These can be used to determine effective values of $u_{\rm a}$, a, L_0 (and hence of $\mathcal{F}$) and of ν and $L_{\rm min}$. The parameters α_1 and β_1 or α_2 and β_2 are then determined as functions of $\mathcal{F}$ and ν by using the curves of Fig. 8.16.

The values of α_1 and β_1 (or α_2 and β_2) for ignition-scale ICF targets are given in Table 8.1. It is seen that in all cases α_1 (or α_2) is close to one. The parameters β_1 and β_2, instead, depend on the driving beam and on the ablator material. In general, β_1 (or β_2) is smaller for indirect drive than for direct-drive. We shall see, however, in § 8.8 that the relevant quantity measuring the effect of ablative stabilization will turn out to be the product of β_2 times the fractional ablated mass. This last quantity is larger for indirect drive than for direct drive so that indirect-drive targets are predicted to be more stable than direct-drive targets. Concerning direct-drive targets, the largest values of β apply to DT ablators. This has lead to the design of targets similar to that illustrated in Chapter 3, but with the outer CH layer replaced by DT or foam-filled DT (Bodner *et al.* 2000; McKenty *et al.* 2001). Table 8.1

8.4.5 *Comparison with experiments and simulations*

Since the beginning of ICF research control of implosion instabilities was recognized as a key issue, and RTI was addressed both analytically and numerically. Lindl and Mead (1975) performed the first 2D simulations of the RTI of the outer surface of a laser-driven shell, showing growth smaller than for classical RTI. These pioneering simulations, however, could not attain the resolution required to investigate complete stabilization. In the early 1980s many authors studied the instability of laser accelerated plane targets, discussing interesting nonlinear effects (see, e. g., McCrory *et al.* 1981; Evans *et al.* 1982). In the same years, experiments provided the first evidence for RTI in laser-driven targets (Cole *et al.* 1982; Grun *et al.* 1982). The quantitative study of ablative stabilization, however, required higher resolution, in both experiments and simulations.

2D simulations proving ablative stabilization at short wavelengths were published in 1990-91 (Tabak *et al.* 1990; Gardner *et al.* 1991). In the following years, RTI growth rates were measured by highly sophisticated experiments. In the remainder of this subsection, we discuss some of these important experimental and numerical results.

Fig. 8.17

The set-up of a typical experiment is shown in Fig. 8.17(a), after Remington *et al.* (1991). It refers to the study of the RTI of a radiation-driven plane target. The X-rays produced in a hohlraum (see Chapter 9) drive a plane foil with an imposed sinusoidal corrugation. Harder X-rays, produced by a backlighter beam (see the top of the figure), are used to probe the accelerated foil. RTI growth is then measured by studying the modulation of the hard X-rays transmitted through the perturbed foil. This allows to obtain space- and time-resolved data on the foil column density $\int \rho dz$. A beautiful example is shown Fig. 8.17(b), where X-ray exposure modulations (related to $\int \rho dz$ modulations) are plotted versus space coordinate at different times. One clearly sees the growth of the modulation. At first modulations are symmetric and roughly sinusoidal. At later times, however, they become asymmetric and the characteristic bubble-and-spike structures appear. The relatively large initial amplitude of the corrugation, however, did not allow to measure linear growth rates.

An important experiment comparing ablative RTI and classical RTI was performed by Budil *et al.* (1996). Two targets were irradiated by identical radiation pulses, producing the same acceleration in both cases. One target was a foil of a single material with a corrugation on the laser side to seed a well defined single-wavelength mode of ablative RTI. The second target consisted of two layers of different materials with the denser one on the side opposite to the laser. The interface between the two materials is unstable to classical RTI. Such an interface was sinusoidally deformed. Different wavelengths were tested for both kinds of targets, and the time integrated growth of the modulation was measured. As shown in Fig. 8.18, substantially different growth curves were obtained in the two cases, clearly showing the difference between ablative and classical RTI.

Fig. 8.18

The measurement of linear growth rates requires control of laser and target parameters to make sure that unperturbed flow parameters, such as accelera-

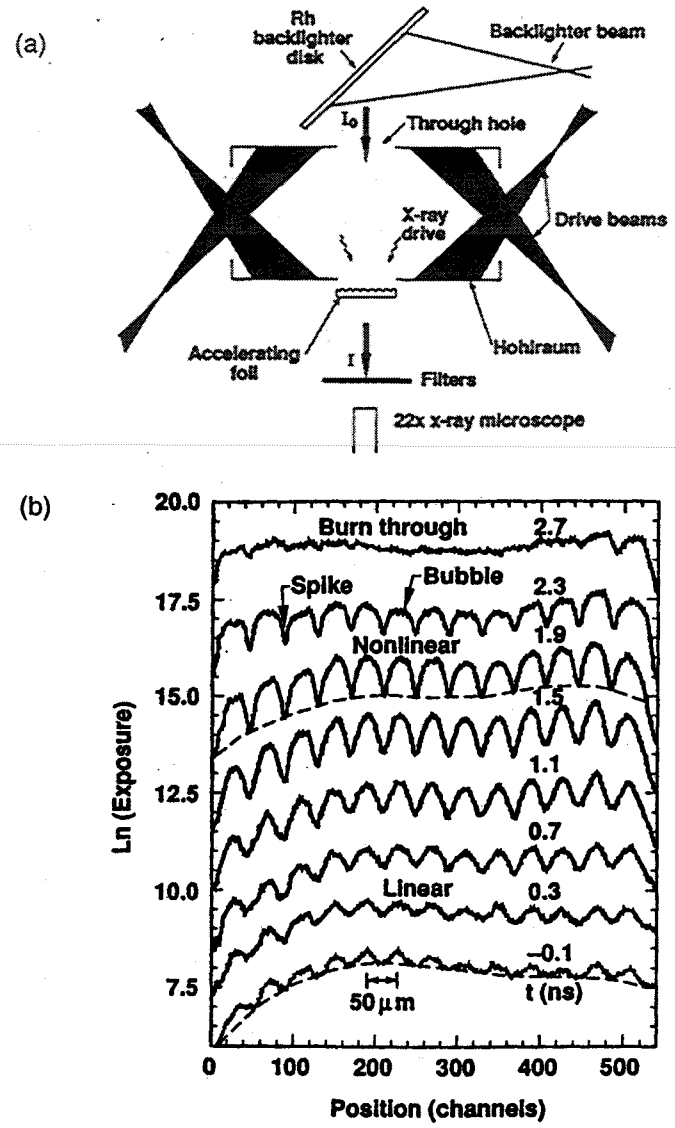

FIG. 8.17. Experiment on RTI of radiation driven foils with imposed sinusoidal perturbation of relatively large amplitude. (a) Experimental set-up. (b) Measured exposure curves versus time for an accelerated thin foil with an initial sinusoidal perturbation with 1.9 μm amplitude and 50 μm wavelength. Each curve represents the average over a 400 ps time interval and is offset vertically from bottom to top in order of increasing time. The dashed curves represent an estimate of the average long-range structure due to backlighter nonuniformity. After Remington *et al.* (1991). Reprinted with permission.

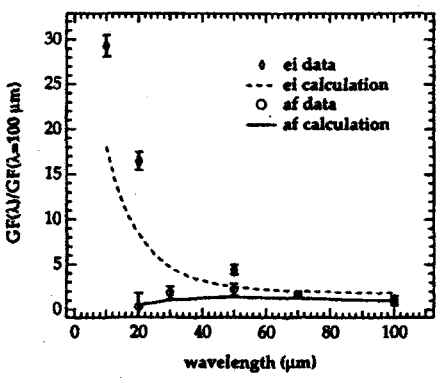

FIG. 8.18. Classical vs ablative RTI growth factors as measured in an experiment by Budil *et al.* (1996). The figure shows the growth factors vs the wavelength of the perturbation. Growth factors are normalized to the measured classical value at $\lambda = 100$ μm. Curves are results of 2D simulations. Reprinted with permission.

tion, are constant in time and that perturbation growth is exponential in time. The growth rates are then obtained by the following procedure. First, mode amplitudes at given times are computed by Fourier transforming X-ray exposure curves such as those shown in Fig. 8.17(b). This allows to obtain the time evolution of the modulation and to check that the amplitude of higher harmonics stays well below that of the imposed mode of perturbation. Finally, growth rates are obtained from the time derivatives of such curves. An example is shown in Fig. 8.19. It refers to 20 μm thick plastic foils, driven by laser pulses with wavelength of 0.53 μm and intensity of 7×10^{13} W/cm^2. The foils have single-mode modulations with different wavelengths λ and different initial amplitudes η_0. The measured foil acceleration is $a = 6 \times 10^{15}$ cm/s^2, and the ablation velocity is about 10^5 cm/s. Frames (a)–(d) show the evolution of the modulation for different values of λ and η_0. A stage of nearly exponential growth is clearly observed. Growth rates vs wavelength are plotted in Fig. 8.19(e). The growth rates are smaller than for classical RTI and agree with 2D simulations. However, the region where full stabilization is expected could not be accessed, because the required space resolution exceeded that experimentally achievable.

Fig. 8.19

Short wavelength stabilization has instead be demonstrated for radiation driven targets by Budil *et al.* (2001). They irradiated 25 μm thick aluminum foils by a pulse of thermal radiation with temperature T_r of about 100 eV. The foils had single-mode modulations with wavelength in the range 10–70 μm. The evolution of foil modulations are shown in Figure 8.20. One sees that perturbations with wavelength of 10 or 12 μm do not grow at all, while those with $\lambda = 16$ μm grow very slowly. Measured modulation evolutions are well repro-

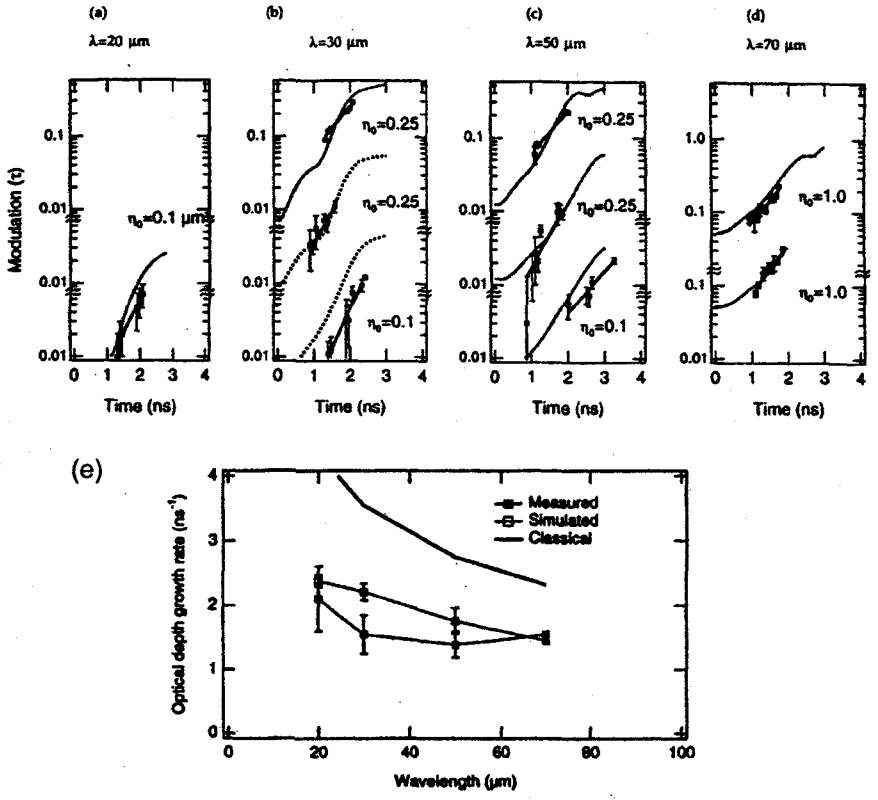

FIG. 8.19. Ablative RTI of a plastic foil driven by a laser pulse. Experiments where performed on foils with initial sinusoidal corrugations. (a)–(d) Amplitude of the modulation of the fundamental mode of optical depth for different wavelengths λ and initial perturbation amplitudes η_0. (e) Average growth rates for different wavelengths compared with the results of simulations and with the classical values. Reduction of the growth rate to 50% of the classical growth rate is observed for $\lambda = 20$ μm and $\lambda = 30$ μm. After Glendinning *et al.* (1997), with permission.

duced by 2D numerical simulations. Fig. 8.20

The above results demonstrate ablative stabilization and good agreement between experiments and simulations. To conclude this subsection, in Fig. 8.21 we compare numerical simulations with theoretical models. Figure 8.21(a) shows data from one of the first studies finding full stabilization at short wavelength (Tabak *et al.* 1990). It refers to a direct-drive target and shows that experimental results are reproduced by Takabe's formula 8.118, with $\alpha_1 = 0.9$ and $\beta_1 = 3$. Figure 8.21(b), instead, refers to an indirectly driven target (Budil *et al.* Fig. 8.21

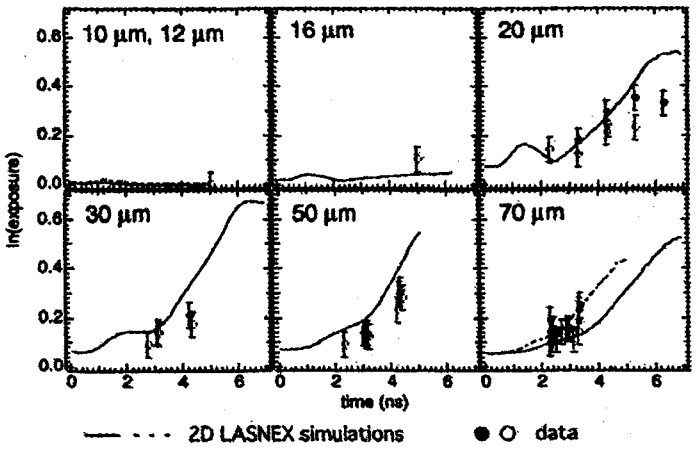

FIG. 8.20. Ablative RTI of radiation driven foils with single wavelength initial perturbations. Growth of the modulation of the optical depth for different values of the wavelength λ. Symbols with error bars represent the amplitude of the exposure modulation. The curves in the figures are results of radiation-hydrodynamics simulations perfomed by means of the 2D LASNEX code. After Budil *et al.* (2001), with permission.

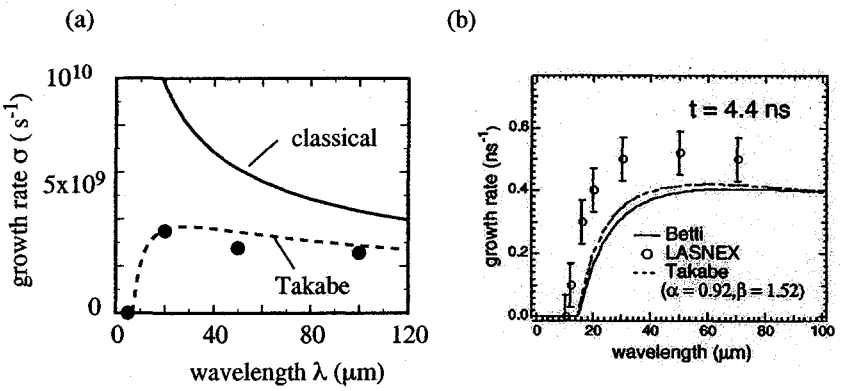

FIG. 8.21. Examples of dispersion relation for ablative RTI obtained by 2D numerical simulations. (a) RTI of a laser-driven CH foil, from LASNEX simulations by Tabak *et al.* (1990). The foil is 20 μm thick and is irradiated by a light pulse with intensity $I = 2 \times 10^{15}$ W/cm^2 and wavelength $\lambda = 0.26$ μm. The dashed curve is Takabe's formula 8.118, with $\beta_1 = 3$. (b) RTI of a 25 μm thick aluminum foil irradiated by thermal radiation with drive temperature $T_r \simeq 100$ eV; after Budil *et al.* (2001), with permission.

2001), with the same parameters as in the experiment of Fig. 8.20. We see that both Takabe's eqn 8.118 and Betti's (or modified-Takabe) eqn 8.119 show the same trends as the numerical results, but do not reproduce the simulation data quantitatively.

8.5 Stability of spherical boundaries

In ICF the Rayleigh-Taylor instability occurs at spherical interfaces rather than at plane boundaries. While convergence effects are negligible at the ablation front, because ablative drive takes place during early stages of implosion when the shell radius is still large, they can be important at the inner surface of the shell when it stagnates at the centre.

In this section, we outline a simplified RTI treatment of an imploding spherical interface and derive two results relevant to ICF, namely i) shell *oscillations* and ii) the linear growth rate for RTI at implosion stagnation. We notice that results presented here are also relevant to many areas of science and technology dealing with collapsing bubbles. These include, e. g., sonoluminescence (Brenner *el al.* 2002), damage of hydraulics machines, and medical application of bubbles [see, e.g. Lohse (2003)].

8.5.1 *Perturbation equation for a cavity*

In this subsection and in the following one we study the evolution of perturbations of an empty spherical cavity. Notice that in the plane ideal RTI we consider stability of an equilibrium state or of a steady state. However when considering converging flows we have to consider the evolution of perturbations of a symmetrical flow, where the unperturbed radius $R(t)$ is an assigned function of time. We then write

$$r(\theta, \phi, t) = R(t) + \zeta(\theta, \phi, t), \tag{8.122}$$

where r is the actual radial coordinate of the perturbed cavity, ζ is the perturbation amplitude, and θ and ϕ are spherical coordinates. In this subsection we shall use potential theory for incompressible flow as in § 8.2. The perturbed potential must then satisfy the Laplace equation 8.5. It is solved in spherical geometry by a superposition of modes

$$\tilde{\varphi}_l \propto \eta^{-j} P_l(\theta), \qquad l = 1, 2, ..., \tag{8.123}$$

where $j = l + 1$ or $j = -l$, and P_l is the spherical harmonic of order l. Since we are interested in the region $r \geq R$ we have to take $j = l + 1$ such that $\tilde{\varphi}_l$ stays finite for $\eta \to \infty$. In addition, the perturbed quantities have to satisfy the kinematic and dynamic boundary conditions at the interface. Here, we omit the detailed treatment, which can be found in the original papers by Bell (1951) and Plesset (1954), and rather quote the main results. It is found that the amplitude ζ_l of the l-th perturbation mode evolves according to

$$\partial_{tt}^2 \zeta_l + 3\frac{\dot{R}}{R}\partial_t \zeta_l - (l-1)\frac{\ddot{R}}{R}\zeta_l = 0. \tag{8.124}$$

The same equation with front factor 2 instead of 3 in the second term on the left hand side applies to cylindrical geometry. Equation 8.124 is known as Bell-Plesset equation. A more transparent equation is obtained by introducing the mass variable $m = \rho R^2/k$, and the wavenumber

$$k = (l+1)/R. \tag{8.125}$$

This gives

$$\partial_t(m\partial_t\zeta_l) - \frac{l-1}{l} m\ddot{R}k\zeta_l = 0. \tag{8.126}$$

Equation 8.126 differs from the equivalent eqn 8.44 for plane geometry, in having a mass varying in time, and in the factor $(l-1)/l$. Equation 8.125 makes apparent that in converging geometries the wavelength $\lambda = 2\pi/k$ of a given perturbation changes as the radius of the cavity changes.

8.5.2 *Stability of a spherical cavity. Cavity oscillations.*

We are now ready to discuss, in qualitative terms, some features of the stability of a spherical cavity. In this context, an important quantity is the amplitude of the perturbation relative to the radius of the cavity, i.e. ζ_l/R. The convergent flow leads to amplification of ζ_l/R even in a cavity collapsing at uniform velocity $\dot{R} = -U$. In this case, $\ddot{R} = 0$, and then eqn 8.126 simply states conservation of $m\partial_t\zeta_l$. For a static initial perturbation (i.e. $\zeta_l = \zeta_{l0}$ and $\partial_t\zeta = 0$ at $t = 0$) of a cavity with initial radius R_0, the amplitude of the perturbation remains constant, but its ratio to the cavity radius grows proportionally to the convergence ratio R_0/R. If $\partial_t\zeta|_{t=0} = \dot{\zeta}_0 \neq 0$, instead, then

$$\zeta_l = \zeta_0 + \frac{1}{2}\frac{\dot{\zeta}_0 R_0}{U}\left(\frac{R_0^2}{R^2} - 1\right), \tag{8.127}$$

showing that even the absolute value of the perturbation is now amplified and diverges as the cavity collapses. Notice that this effect is independent of the mode number.

To examine a case in which the cavity is accelerated inwards, we refer to the so-called ballistic motion of an imploding cavity, i.e. to an implosion occurring at fixed kinetic energy. This is described by (Kull 1991)

$$\dot{R}/R = -(2/5)/(t_c - t), \qquad \ddot{R}/R = -(6/25)/(t_c - t)^2, \tag{8.128}$$

where t_c is the time at which the cavity collapses. In this case the solution of eqn 8.124 is

$$\zeta_l = \left(\frac{R_0}{R}\right)^{1/4}\zeta_{l0}\left[\cos(\xi s) - \left(\frac{1}{4} + \frac{\dot{\zeta}_0}{\dot{R}_0}\frac{R_0}{\zeta_0}\right)\frac{\sin(\xi s)}{\xi}\right], \tag{8.129}$$

where

$$\xi = \xi(l) = \sqrt{(3/2)(l-1) - (1/16)}, \qquad s = s(t) = \ln[R_0/R(t)]. \tag{8.130}$$

We see that in addition to the amplification of the perturbation by a factor $(R_0/R)^{1/4}$, the cavity undergoes *oscillations* depending on the product $\xi(l)s(t)$, which is a function of both mode number and time.

A more general criterion for the stability of an imploding spherical or cylindrical shell, implying that the solution of eqn 8.126 (or the analogous equation for cylindrical geometry) remains finite, was presented by Birkhoff (1954). It reads

$$\ddot{R} < 0 \quad \text{and} \quad R(d^3R/dt^3) + (2\delta - 1)\dot{R}\ddot{R} < 0 \tag{8.131}$$

with $\delta = 3$ or 2 for spherical and cylindrical geometry, respectively. The first condition holds in general and just states that the interface is Rayleigh-Taylor stable if the acceleration is directed from the fluid to the void. The second one, instead, is specific to the converging geometry. An interesting point is that incompressible converging flows ($\dot{R} < 0$) with constant inward acceleration ($\ddot{R} = \ddot{R}_0 < 0$) are unstable, even in the case when there is no RTI.

8.5.3 *Classical RTI at implosion stagnation*

In the previous subsections we have considered the stability of imploding void cavities. In fact, in ICF and other applications one deals with a spherical interface separating two fluids of different densities. Here, we show that the linear growth rate of the perturbations of a stagnating spherical interface is well approximated by the expression for the classical RTI of a plane interface.

A classical treatment of the problem is due to Bell (1951) and Plesset (1954), who considered the implosion of the spherical interface separating an outer incompressible fluid with density ρ_2, filled with another incompressible fluid with density ρ_1. Of course, the assumption of incompressibility of the filling gas requires the presence of a sink or a source at the origin. Despite these evidently rough assumptions, the model proves quite accurate, as it is confirmed by numerical studies. The equation for the evolution of the perturbations now reads

$$\partial_{tt}^2\zeta_l + 3\frac{\dot{R}}{R}\partial_t\zeta_l - \frac{l(l-1)\rho_2 - (l+1)(l+2)\rho_1}{l\rho_2 + (l+1)\rho_1}\frac{\ddot{R}}{R}\zeta_l = 0, \tag{8.132}$$

from which eqn 8.124 is recovered when $\rho_1 = 0$. We stress that the interface trajectory is prescribed and therefore $R(t)$, $\dot{R}(t)$, and $\ddot{R}(t)$ are known functions of the time.

Important insight is obtained from an approximate solution of eqn 8.132. By introducing the new variable

$$y_l = (R/R_0)^{3/2}\zeta_l, \tag{8.133}$$

with R_0 being an arbitrary value of the interface radius, eqn 8.132 transforms into the equivalent equation

$$\partial_{tt}^2 y_l + G_l(t)y_l = 0, \tag{8.134}$$

where

$$G_l(t) = -\frac{3}{4}\frac{\dot{R}^2}{R^2} - \frac{\ddot{R}}{R}\left[\frac{3}{2} + \frac{l(l-1)\rho_2 - (l+1)(l+2)\rho_1}{l\rho_2 + (l+1)\rho_1}\right]. \tag{8.135}$$

Equation 8.134 can be solved in the WKB approximation (see § 1.2.3 and the references therein quoted) which gives

$$\zeta_l = \left(\frac{R_0}{R}\right)^{3/2} y_l \approx \left(\frac{R_0}{R}\right)^{3/2} \frac{1}{|G_l|^{1/4}} \exp\left(\pm i \int G_l^{1/2} dt\right). \tag{8.136}$$

One sees that the perturbation grows nearly exponentially in time, if $G^{1/2}$ has an imaginary part, i.e. if the real function G is negative.

The solution becomes particularly simple and enlightening just in the case of greatest interest for ICF, i.e. that concerning *instability at the time of stagnation* (see Fig. 8.1). In this case $\dot{R} \simeq 0$, and for relatively large values of l, $G_l \simeq -lA_t\ddot{R}/R = -\ddot{R}k_{\rm eff}A_t$, where $k_{\rm eff} = l/R$ is an effective wavenumber and $A_t = (\rho_2 - \rho_1)/(\rho_2 + \rho_1)$ is the instantaneous value of the Atwood number. For a dense stagnating shell, $A_t > 0$, and then perturbations grow in time according to

$$\zeta_l \approx \left(\frac{R_0}{R}\right)^{3/2} (\ddot{R}k_{\rm eff}A_t)^{-1/4} \exp \int (\ddot{R}k_{\rm eff}A_t)^{1/2} dt. \tag{8.137}$$

Neglecting the weak time dependence of the front factor, the perturbation grows exponentially with a growth rate

$$\sigma = \sqrt{\frac{lA_t\ddot{R}}{R}} = \sqrt{\ddot{R}k_{\rm eff}A_t} \tag{8.138}$$

equal to the classical RTI expression 8.36.

Recently, Amendt *et al.* (2003) have modified the Bell-Plesset model, including the effect of compressibility of both fluids. It is interesting to notice that, while compressibility is in general important, its effect on RTI at stagnation turns out to be small. Indeed, according to their treatment, the growth rate at stagnation is simply obtained by multiplying eqn 8.138 by the factor $\{1 + (\alpha_c/l)[\rho_2/(\rho_2 - \rho_1)]\}^{1/2}$, where $\alpha_c = -(R/\dot{R})(\dot{\rho}_2/\rho_2)$ is a dimensionless compressibility parameter, typically in the range of 2–3. For $l \gg 1$ the correction to the Bell-Plesset growth rate is therefore negligible.

Numerical solutions of the perturbations equations, including the effect of compressibility and using the radial motion $R(t)$ obtained from self-similar implosion solutions, indeed confirm the accuracy of eqn 8.138 (Hattori *et al.* 1986).

8.5.4 *Ablative RTI of decelerating ICF shells*

The RTI occurring during deceleration and stagnation of an ICF target differs from classical RTI discussed in the previous subsections. Indeed the heat flow

and the flow of α- particles from the central hot spot cause ablation of the decelerating dense shell. Although this effect has been known for a long time (and is discussed, e.g., in Chapters 3 and 4), only recently Lobatchev and Betti (2000) have pointed out that it stabilizes RTI. They have shown that the linear growth rate of the relevant deceleration-phase ablative RTI is well approximated by the same expression 8.119 which applies to the RTI of a beam-driven ablation front. We then have

$$\sigma \simeq \left(\frac{\ddot{R}l/R}{1 + L_{\rm in} l/R} \right)^{1/2} - \beta_{\rm in} \frac{l}{R} u_{\rm ain}, \tag{8.139}$$

where we have used $k = l/R$. Here $L_{\rm in}$ is the minimum density scale-length at the hot spot surface, $u_{\rm ain}$ is the ablation velocity of the inner shell surface and $\beta_{\rm in} \simeq 1.5$ is a numerical coefficient. Further details can be found in a paper by Atzeni and Temporal (2003), who analyze the stabilizing role of the different transport mechanisms. In concluding this section, it is worth mentioning that recent progress in diagnostic techniques have allowed for the first direct experimental measurements of the time evolution of the deformation of an ICF shell during the stages of deceleration and stagnation (Smalyuk *et al.* 2002).

8.6 Nonlinear evolution of single-mode perturbations

In the previous sections we have discussed the behaviour of small amplitude perturbations. In the case of plane interfaces we considered modes of sinusuoidal shape. As shown in Fig. 8.4, larger disturbances have substantially different behaviour. Their shape is no more symmetrical, and the time evolution is no more exponential. In this section, we study the nonlinear evolution of a single wavelength perturbation. First, in § 8.6.1, we study analytically the evolution of a rising bubble. We will compute the speed of the bubble vertex and the bubble radius of curvature at all stages of the evolution. The asymptotic behaviour of RTI and RMI bubbles and spikes for any value of the Atwood number $A_{\rm t}$ is then studied in § 8.6.2. The results of § 8.6.2 allow to derive a simple criterion for growth saturation, which is presented in § 8.6.3. Finally, in § 8.6.4 we discuss qualitatively the difference between 2D and 3D perturbations.

Notice that bubble penetration into the heavy fluid is relevant to RTI at the outer surface of an ICF target: during acceleration, it is just the penetration of the light plasma bubbles into the accelerated solid layer that could lead to shell rupture. Spikes of the dense shell material can instead penetrate into the hot spot during the unstable collapse stage, degrading ignition.

8.6.1 *RTI bubble evolution for* $A_{\rm t} = 1$

Here, we discuss bubble evolution, following an elegant treatment presented by Layzer (1955). We use the potential flow model of an incompressible fluid and refer to a semi-infinite fluid ($A_{\rm t} = 1$), subject to downward directed gravity or to upward directed acceleration a and supported by a uniform pressure. We further

assume 2D x-z slab geometry with periodic boundary conditions in x having wavelength $\lambda = 2\pi/k$ and take a reference system moving with the bubble vertex, which has height $h_b(t)$ relative to the position of the unperturbed boundary. By definition, $u_z = 0$ at the vertex ($x = z = 0$), which moves with the fluid. The bubble surface is described by $z = \zeta(x,t)$.

The model is based on the ansatz for the velocity potential

$$\varphi(x,z,t) = \varphi_1(t)\left[e^{-kz}\cos(kx) - 1 + kz\right], \tag{8.140}$$

which is certainly a solution of the Laplace equation $\nabla^2\varphi = 0$ and has the velocity components

$$u_x = \partial_x\varphi = -k\varphi_1(t)e^{-kz}\sin(kx), \tag{8.141}$$

$$u_z = \partial_z\varphi = k\varphi_1(t)\left[e^{-kz}\cos(kx) + 1\right]. \tag{8.142}$$

They satisfy the boundary conditions, at least $u_x = 0$ at $x = \pm\lambda/2$, $u_z = 0$ at the vertex ($x = z = 0$), and

$$\lim_{z\to\infty} u_z = k\varphi_1(t) = -\dot{h}_b, \tag{8.143}$$

far ahead of the front, where the fluid mass moves with the negative velocity of the reference frame. Potential 8.140 may be considered as the first term of a Fourier expansion of the real potential. It does not fully satisfy the equations

$$\left[\partial_t\zeta + u_x\partial_x\zeta - u_z\right]_{z=\zeta(x,t)} = 0, \tag{8.144}$$

$$\left[\partial_t\varphi + u^2/2 + (a + \ddot{h}_b)z\right]_{z=\zeta(x,t)} = 0 \tag{8.145}$$

everywhere at the interface $z = \zeta(x,t)$, but we use them in the neighborhood of $x = z = 0$ to determine the velocity and curvature of the bubble at the vertex. Equations 8.144 and 8.145 are derived from eqs 8.14 and 8.8, respectively; the integration constant of eqn 8.8 has been evaluated at the vertex and is $C(t) = 0$.

Making use of eqns 8.140–8.143, the interface equations 8.144 and 8.145 become, respectively,

$$\partial_t\zeta + \dot{h}_b(e^{-k\zeta}\partial_x\zeta\sin kx + 1 - e^{-k\zeta}\cos kx) = 0 \tag{8.146}$$

and

$$\ddot{h}_b(1 - e^{-k\zeta}\cos kx) + \frac{1}{2}\dot{h}_b^2 k(1 - 2e^{-k\zeta}\cos kx + e^{-2k\zeta}) + ak\zeta = 0. \tag{8.147}$$

Following Layzer (1955), we look for solutions satisfying them in a neighborhood of the bubble vertex (i.e. the origin $x = z = 0$ of our coordinate system). To this purpose, we expand the equation for the bubble surface as

$$\zeta(x,t) = -\frac{1}{2}\frac{C_\zeta(t)}{k}(kx)^2 + O[(kx)^3], \tag{8.148}$$

where C_ζ is a normalized curvature radius. Consistently, we expand $\cos(kx)$, $\sin(kx)$, $\exp(kx)$ $\exp(k\zeta)$, etc. in eqns 8.146 and 8.147 up to second order in kx. This leads to

$$\dot{C}_\zeta - k\dot{h}_b(1 - 3C_\zeta) = 0, \tag{8.149}$$

$$\ddot{h}_b + \frac{\dot{h}_b^2 k}{1 - C_\zeta} - a\frac{C_\zeta}{1 - C_\zeta} = 0. \tag{8.150}$$

~~Equation 8.150~~ For $h_b \ll 1/k$, eqn 8.150 reduces to $\ddot{h}_b = aC_\zeta = kah_b$, i.e. $h_b \propto \exp(\sqrt{kat})$ which reproduces the classical RTI linear solution. In the opposite limit of a large bubble amplitude, eqns 8.149 and 8.150 show, instead, that the bubble rises with constant normalized curvature $C_\zeta(t) = C_\zeta^{as} = 1/3$ and constant velocity

$$u_b^{as} = \dot{h}_b^{as} = \sqrt{\frac{aC_\zeta^{as}}{k}} = \sqrt{\frac{a\lambda}{6\pi}} = 0.23\sqrt{a\lambda}. \tag{8.151}$$

A similar analysis (Layzer 1955) shows that the asymptotic rise velocity of a cylindrically symmetric bubble of diameter D is

$$u_b^{as-cyl} = 0.361\sqrt{aD}. \tag{8.152}$$

It is important to observe that larger bubbles rise more rapidly ($u_b^{as} \propto \lambda^{1/2}$) than smaller bubbles, while in the linear regime they had smaller growth rate, according to $\sigma \propto \lambda^{-1/2}$ (see Fig. 8.22).

Further information on the time evolution of bubble curvature and velocity can be obtained as follows. Equations 8.149 and 8.150 can be integrated once analytically, for initial conditions $C_\zeta(t = 0) = C_0$, $h_b(t = 0) = h_0$, and $\dot{h}_b(t = 0) = \dot{h}_0$. Integrating eqn 8.149 by parts, we get

$$C_\zeta = C_\zeta(h_b) = \frac{1}{3}\left\{1 - A_1 e^{-3k(h_b - h_0)}\right\}, \tag{8.153}$$

where $A_1 = 1 - 3C_0$. Integration of eqn 8.150 is less straightforward. Setting $s = \dot{h}_b^2$, one has $\ddot{h}_b = d\dot{h}_b/dt = \dot{h}_b(d\dot{h}_b/dh_b) = (1/2)d\dot{h}_b^2/dh_b = (1/2)ds/dh_b$. Equation 8.150 then becomes

$$\frac{ds}{dh_b} + \frac{2k}{1 - C_\zeta}s = 2a\frac{C_\zeta}{1 - C_\zeta}, \tag{8.154}$$

which is a first order linear equation for $s(h_b)$. It can be solved by the method of integrating factors, multiplying each term by $\exp[(2kh_b)/(1 - C_\zeta)]$. After some algebra one finds (Kull 1983)

$$\dot{h}_b^2 = \frac{(2a/3k)(1 - G) - G\left[2aA_1(h_b - h_0) - \dot{h}_0^2(2 + A_1)\right]}{2 + A_1 G}, \tag{8.155}$$

where $G = \exp[-3k(h_b - h_0)]$.

Fig. 8.22

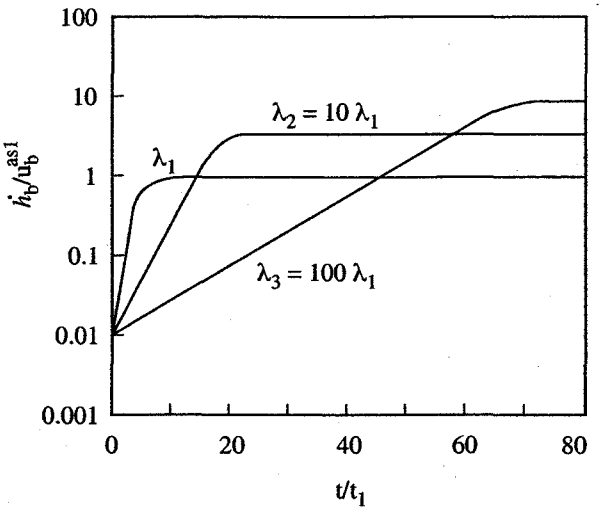

FIG. 8.22. Bubble rise velocity vs time for different bubble wavelengths and the same initial conditions: smaller bubbles have faster linear growth, but smaller asymptotic velocity. Here time is normalized to $t_1 = 1/\sqrt{(ak_1)}$, with $k_1 = 2\pi/\lambda_1$.

	RTI	RMI
bubble	$u_b^{as} = \sqrt{\frac{2A_t}{1+A_t}}\sqrt{\frac{a\lambda}{6\pi}}$	$u_b^{as} = \frac{1}{6\pi}\frac{3+A_t}{1+A_t}\frac{\lambda}{t}$
spike $A_t = 1$	$\dot{u}_s^{as} = -a$	$u_s^{as} = -\lvert u_0\rvert\sqrt{\frac{-3C_0+3}{-3C_0+1}}$
spike $A_t < 1$	$u_s^{as} = -\sqrt{\frac{2A_t}{1-A_t}\frac{a\lambda}{6\pi}}$	$u_s^{as} = -\frac{1}{6\pi}\frac{3-A_t}{1-A_t}\frac{\lambda}{t}$

Table 8.2 *Asymptotic bubble and spike behaviour for RTI and RMI (in Cartesian geometry). C_0 is the normalized bubble curvature immediately after shock transit through the interface.*

8.6.2 *Asymptotic bubble and spike behaviour for arbitrary A_t*

The expressions of the asymptotic RMI and RTI bubble and spike velocities are listed in table 8.2 for arbitrary values of the Atwood number A_t. For $A_t = 1$, the RTI bubbles are described by the model discussed in the previous subsection; RMI bubbles and RTI and RMI spikes are dealt with by similar treatments (Zhang 1998). All results of Table 8.2, except that for the asymptotic velocity of an RMI spike for $A_t = 1$ are recovered by a simple model. Here we follow Alon *et al.* (1995) and Shvarts *et al.* (2001). A critical discussion of the model can be found in a review article by Dimonte (2000).

For the RTI bubble, one applies Newton's law to the fluid volume V just above the interface

$$(2\rho_2 V + \rho_1 V)\frac{du_b}{dt} = (\rho_2 - \rho_1)aV - C_{drag}\rho_2 u_b^2 S, \tag{8.156}$$

expressing the fact that the bubble is accelerated upwards by the buoyancy force due to the difference in density between the two fluids and slowed down by the drag exerted on it by the heavier fluid. Here, as in previous sections of this chapter, ρ_2 and ρ_1 are the densities of the two fluids. The two terms in the parenthesis on the left hand side are interpreted by Shvarts *et al.* (2001) as *added mass* and *inertia*, respectively. The drag contribution is $F_d = -C_{drag}\rho_2 u_b^2 S$, where C_{drag} is a numerical coefficient and S is the area of the bubble cross-section. Estimating $V/S \simeq \lambda$, we have

$$u_b^{as} = \left(\frac{2A_t}{1+A_t}\right)^{1/2}\left(\frac{2}{3C_{drag}}a\lambda\right)^{1/2}. \tag{8.157}$$

For $A_t = 1$, we recover eqn 8.151, setting $C_{drag} = 6\pi$.

Equation 8.156 with $a = 0$ can also be used to evaluate the asymptotic behaviour of the RMI bubbles, for which we get

$$u_b^{as\ RM} = \frac{1}{C_{drag}}\frac{3+A_t}{1+A_t}\lambda/t, \tag{8.158}$$

For the spikes, instead, one can write

$$(2\rho_1 V + \rho_2 V)\frac{du_s}{dt} = -(\rho_2 - \rho_1)aV + C_{drag}\rho_1 u_s^2 S, \tag{8.159}$$

which yields the expressions for the asymptotic acceleration $\dot{u} = -a$ of the $A_t = 1$ RTI spike, and for the asymptotic velocities of RMI and RTI spikes printed in the last line of Table 8.2. We see that RTI spikes fall at constant acceleration for $A_t = 1$, and at constant velocity for $A_t < 1$. RMI spikes, instead, fall at constant velocity for $A_t = 1$, while their velocity vanishes $\propto 1/t$ for $A_t < 1$.

8.6.3 *Saturation amplitude of a single RTI mode*

Applications of RTI theory require a simple criterion for saturation, indicating the maximum amplitude of the perturbation which can still be dealt with by linear theory. A simple condition can be obtained from the results for the asymptotic evolution of a bubble. We assume that saturation occurs when the perturbation velocity predicted by linear theory, $\dot{\zeta} = \sigma_{RT}\zeta$, equals the asymptotic bubble velocity given by eqn 8.157. The corresponding *saturation amplitude* is

$$\zeta^{sat} = \frac{\lambda}{2\pi\sqrt{3}}\sqrt{\frac{2}{A_t+1}} \simeq 0.1\lambda\sqrt{\frac{2}{A_t+1}}. \tag{8.160}$$

More rigorously, the formation of asymmetric bubble-spike shapes and the onset of saturation are shown by third-order perturbation theory (Jacobs and

Catton 1988); the result is that an initial perturbation $\zeta_0(x,t) = \zeta_{10}\cos(kx)$ of an interface with $A_t = 1$ evolves according to

$$\zeta(x,t) = \zeta_1^{\rm Lin}\left\{[1 - \frac{1}{4}\left(k\zeta_1^{\rm Lin}\right)^2]\cos kx \right. \\ \left. -\frac{1}{2}(k\zeta_1^{\rm Lin})\cos 2kx + \frac{3}{8}(k\zeta_1^{\rm Lin})^2\cos 3kx\right\}. \qquad (8.161)$$

Here $\zeta_1^{\rm Lin} = \zeta_{10}\cosh(\sigma_{\rm RT}t)$ is the amplitude of the fundamental mode as given by the linear theory and $\sigma_{\rm RT}$ is the classical RTI growth rate. Equation 8.161 shows that the second order term makes the shape asymmetric, since the height of the rising vertex is $\zeta_1 - k\zeta_1^2/2$ and the depth of the falling vertex is $\zeta_1 + k\zeta_1^2/2$. The third order term not only generates a third harmonic, but also reduces the growth rate of the fundamental mode. We see that for $\zeta_1/\lambda = 0.1$, i.e. $k\zeta_1 = 0.2\pi$, the amplitude of the fundamental mode is reduced by about 10% and the second harmonic and the third harmonic are about 1/3 and 1/10 as large as the fundamental one, respectively. At this stage, linear theory is no more applicable.

8.6.4 *3D vs 2D nonlinear RTI evolution*

Actual surface perturbations are three-dimensional. We have seen in § 8.2.5 that the linear evolution of a single wavelength perturbation of a plane surface depends only on the wavenumber, which allowed us to restrict ourselves to 2D perturbations without any loss of generality. The case is different, however, when the amplitude of the perturbations grows. We have indeed already seen (see eqns 8.152 and 8.151) that the asymptotic rise velocity of a 2D slab bubble is smaller than that of a cylindrically symmetric bubble with the same cross section. Most insight in the evolution of 3D perturbations has been obtained from numerical simulations. Here we summarize some findings of general interest.

First of all, one observes topological differences. In 2D, the perturbed surface appears as a sequence of bubbles and spikes, with each spike fed by fluid coming from the top of two adjacent bubbles. In 3D, instead, each bubble (spike) is adjacent to several spikes (bubbles). The formation of bubbles and spikes is shown in Fig. 8.23. The figure shows the results of a 3D simulation performed by a code developed by M. Temporal at INFN Legnaro in collaboration with ENEA-Frascati. Deeply in the nonlinear regime, the shape of a deformed interface is therefore substantially different from that obtained from 2D simulations. An example is given in Fig. 8.24, which also refers to a single mode 3D perturbation of a plane interface. Typically, 3D bubbles have a larger boundary area to feed the spike than in the 2D case. This explains why cylindrical bubbles saturate at larger amplitude than 2D Cartesian bubbles (see § 8.6.1).

Fig. 8.23

Fig. 8.24

Simulations also show that in both classical and ablative RTI the mushroom structure owing to KHI is much smaller in 3D than in 2D (see Fig. 8.25). Spikes are then thicker and grow faster in 3D than in 2D (Yabe *et al.* 1991). An explana-

Fig. 8.25

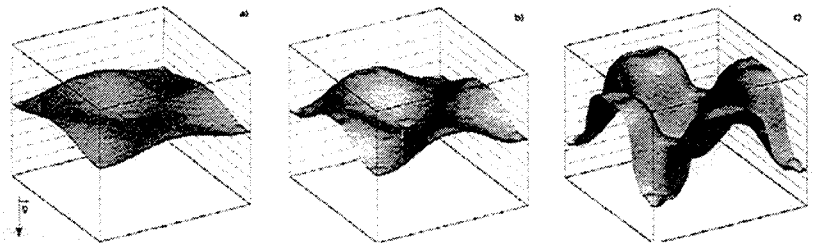

FIG. 8.23. Growth of a single mode 3D perturbation, with $k_x = k_y$.

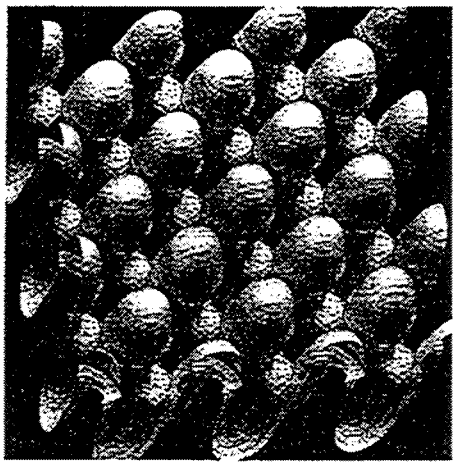

FIG. 8.24. Plane interface between two fluids, for a single mode 3D perturbation during the nonlinear stage. The Atwood number of the interface is 0.5. The interface is seen form the bubble side. After Hecht *et al.* (1995), with permission.

tion for this effect has been given in terms of a secondary instability developing around the already deformed interface (Dahlburg and Gardner 1990). Vortex rings appear in both 2D and 3D, but while in 2D they are confined in a plane, in 3D they can tilt and stretch. The altered flow pattern generated by dynamic tilting serves to pump additional mass into the sides of the growing spike. Vortex stretching and tilting can also trigger turbulent behaviour.

In conclusion, the asymptotic nonlinear evolution of single-wavelength perturbations is faster in 3D than in 2D. Concerning applications to ICF, however, one should recall (see the discussion of § 8.1.2) that RTI growth has to be limited to the early nonlinear stage in this context, where differences between 2D and 3D evolution are small.

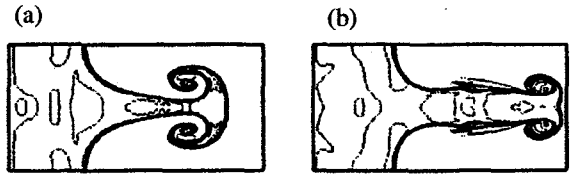

FIG. 8.25. Nonlinear stage of the single-mode RTI of a plane interface with Atwood number $A_t = 0.54$. (a) 2D plane perturbation; (b) 3D perturbation. After Yabe *et al.* (1991), with permission.

8.7 Nonlinear evolution of multi-mode perturbations

8.7.1 *Preview and relevance to ICF targets design*

Real surfaces are characterized by perturbations having a broad Fourier spectrum of modes. As far as the amplitude of the unstable perturbations is small, one can use linear theory and compute the evolution of the global perturbation. It results from the superposition of independent modes, each characterized by its own growth rate. Beyond the linear stage a number of new features are observed, which do not occur in the nonlinear growth of a single mode. For instance, we may refer to Fig. 8.5, showing frames from a 2D simulation of the classical RTI of an interface with an initially flat shape and velocity perturbation consisting of 19 sinusoidal modes, having dimensionless wavelength $\lambda_n = 1/n$ with $n = 41, 42, ..., 59$. The velocity perturbations have random initial amplitudes in the interval $0 \leq \zeta_n(t = 0) \leq 2 \times 10^{-3}$. In this simulation, lengths are normalized to the wavelength of the fundamental mode and times to the reciprocal of the classical RTI growth rate of the fundamental mode. We observe that the perturbed interface first shows a large number of bubbles and spikes of small scale and relatively simple structure and later a smaller number of much larger bubbles and complex flow patterns. The region of fluid affected by the instability grows in time. At later times a nearly chaotic behaviour occurs, leading to *turbulent mixing*.

The evolution, observed in Fig. 8.5 for the classical RTI of superimposed fluids, in principle occurs for ablative RTI, too. An example is shown in Fig. 8.26, referring to a 2D simulation of RTI of an ablatively driven foil with initial random perturbation. As seen from frame (a), the initial perturbation has relatively large amplitude, so that the evolution soon becomes nonlinear. After a stage of coexistence, bubbles compete. Small bubbles are washed downstream, while larger bubbles run through the target.

Fig. 8.26

It appears that mode coupling and bubble competition are general features of nonlinear evolution. However, these two effects do not play a significant role in ICF targets designed to achieve ignition. There are two main reasons for this, discussed in detail by Haan (1991). First, modes with very short wavelength, which saturate and couple nonlinearly very soon in classical RTI, are stable in ablative RTI. In addition, we have already seen that successful implosion of thin ICF shells requires that the amplitude of the potentially most damaging

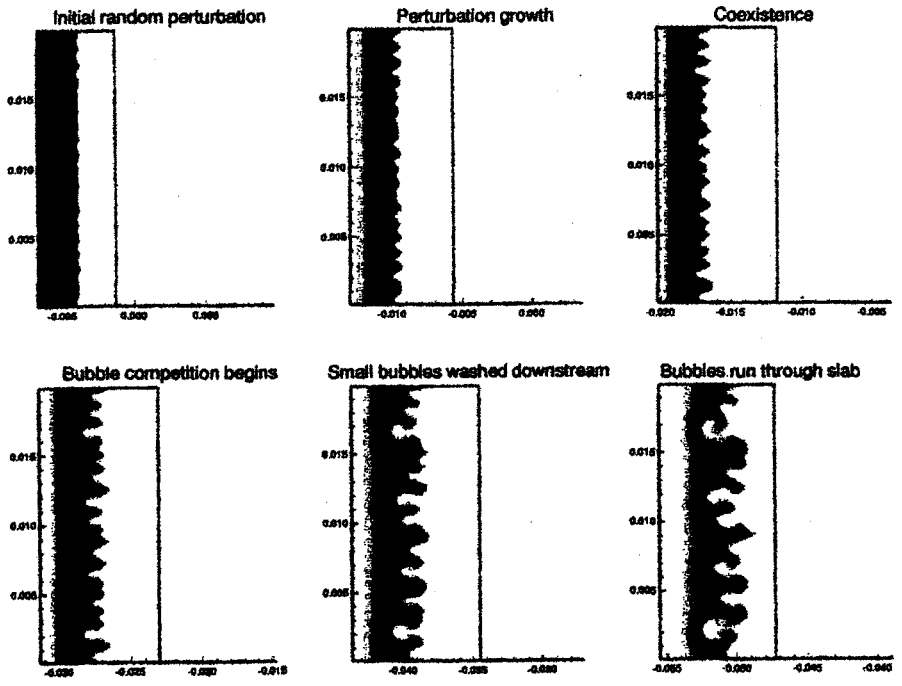

FIG. 1.26. Ablative RTI of a laser-accelerated foil with initial random perturbation. The foil is irradiated by a laser pulse coming from the right-hand side. After Oron *et al.* (1998), with permission.

modes can only slightly exceed their respective saturation thresholds. This means that the fully nonlinear stage of evolution must be avoided anyhow in ICF. On the other hand, saturation of linear growth and the early stages of nonlinear evolution are important in ICF target design. These topics are discussed in the next subsections.

8.7.2 *Growth saturation of a full spectrum of modes*

When dealing with a full spectrum of modes, an important question concerns the amplitude at which each individual mode saturates. Here we closely follow the beautiful presentation by Hoffman (1995), who discussed the treatment due to Haan (1989). We start by observing that a group of modes with nearly equal wavevectors can combine constructively over a region of the interface, producing a structure whose amplitude is much larger than the amplitudes of each of the individual modes. We expect that such a structure saturates when its net amplitude is a fraction $C_\zeta \approx 10\%$ of its effective wavelength, as in the case of a single sinusoidal mode ($A_t = 1$ is assumed here). At this stage, however, the individual modes composing the structure have amplitudes much smaller than

10% of their wavelength, which means that they saturate earlier than we would expect for the single mode saturation. The key point of the model for the evaluation of saturation amplitudes is that one cannot distinguish a pure mode from a superposition of many modes, unless one performs a measurement over a large spatial region, having a width sufficient for dephasing of individual modes.

Haan's model applies this principle to a broad spectrum and makes the basic assumption that the modes $\mathbf{k}'$ interacting constructively with a given mode $\mathbf{k}$ are those satisfying $|\mathbf{k}-\mathbf{k}'| < \epsilon|\mathbf{k}|$, i.e. are contained in a circle of radius ϵk centered on $\mathbf{k}$. We call $N_k = N(\epsilon, k)$ the number of such modes. Here ϵ is a parameter with a numerical value of about 0.3. These modes combine to produce a perturbation with approximate wavelength $\lambda = 2\pi/k$ and root-mean-square amplitude $\zeta_{\rm rms}$. It will saturate when it reaches a peak amplitude $\sqrt{2}\zeta_{\rm rms} = C_\zeta \lambda$, i.e. when $k\zeta_{\rm rms} = \sqrt{2}\pi C_\zeta$. Assuming that modes have random phases and nearly equal amplitudes, one obtains

$$\zeta_{\rm rms}^2 = \sum_{|\mathbf{k}-\mathbf{k}'|<\epsilon|\mathbf{k}|} \zeta_{k'}^2 \simeq N_k \zeta_k^2. \tag{8.162}$$

To compute N_k we refer to a plane interface with dimensions $L \times L$, where the allowed components of $\mathbf{k}'$ have $k_x' = 2\pi n/L$ and $k_y' = 2\pi m/L$ with $n = 1, ..., \infty$ and $m = 1, ..., \infty$. The number of modes is then given by twice the product of the area of the circle $\pi(\epsilon k)^2$ times the density of states $(L/2\pi)^2$. Using this result we find that at saturation the amplitude of the mode with wavenumber k satisfies

$$k\zeta_k^{\rm sat} = 2\pi^{3/2}(C_\zeta/\epsilon)(kL)^{-1}, \tag{8.163}$$

which can also be written as

$$\zeta_k^{\rm sat} = \frac{1}{2\sqrt{\pi\epsilon}}(C_\zeta\lambda)\frac{\lambda}{L} \simeq 0.1\lambda\frac{\lambda}{L}. \tag{8.164}$$

It shows that higher modes saturate at an amplitude smaller by a factor λ/L than that given by the single mode criterion, eqn 8.160.

Equation 8.164 can easily be generalized to spherical geometry by setting $L = 2R$ and $\lambda = 2\pi R/l$, where l is the spherical harmonic mode number, which gives

$$\zeta_l^{\rm sat} \simeq 2\frac{R}{l^2}. \tag{8.165}$$

Fig. 8.27

In Fig. 8.27 saturation levels predicted by eqn 8.165 are compared with those obtained from the single mode criterion $\zeta_l \simeq 0.1\lambda_l = 0.2\pi R/l$. Again, a large difference is observed at large l. In practice, the saturation amplitude employed in simple RTI growth evaluations is the smallest between single- and multi-mode values.

8.7.3 *Model for weakly nonlinear evolution after saturation*

A simple model, developed by Haan (1989), describes the evolution of the perturbations in the early stages after saturation. It can be applied when second-order

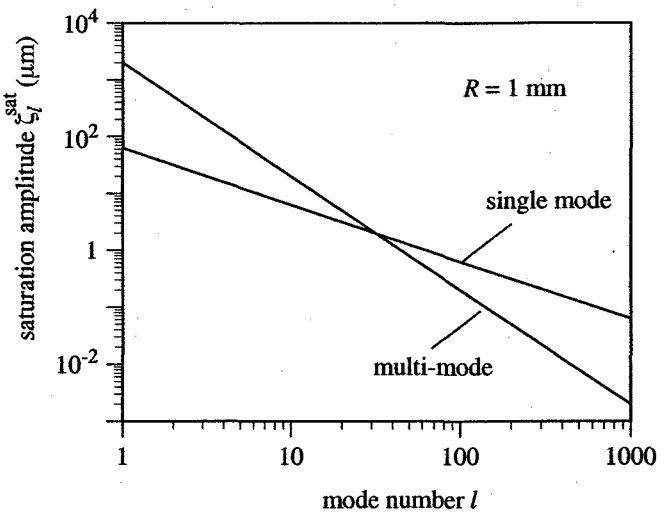

FIG. 8.27. Saturation amplitudes versus mode number l as predicted by the single mode treatment (eqn 8.160) and by the multi-mode criterion (eqn 8.165) for a spherical interface with radius $R = 1$ mm.

mode coupling has negligible effects (see the discussion at the end of § 8.7.1). This model is widely used by ICF target designers to estimate the overall growth of the perturbation at the outer surface of a capsule.

The model is built on two elements. The first one is the saturation criterion discussed in the previous subsection. The second is the assumption that after saturation each mode grows independently of the other modes with a rate analogous to that of Layzer's periodic bubbles (see § 8.6.1).

According to this model, the growth velocity of a perturbation with wavenuber k is given by linear theory if the amplitude of the perturbation has not yet achieved the saturation threshold ζ_k^{sat}, while it is constant afterwards:

$$\frac{d\zeta_k(t)}{dt} = \begin{cases} \sigma_k \zeta_k & \text{for } \zeta_k \le \zeta_k^{sat}, \\ \sigma_k \zeta_k^{sat} & \text{for } \zeta_k \ge \zeta_k^{sat}, \end{cases} \tag{8.166}$$

where $\sigma_k = \sigma(k)$ is the relevant linear growth rate. For constant growth rate σ_k, eqn 8.166 can be integrated analytically, which gives

$$\zeta_k(t) = \begin{cases} \zeta_k^{lin}(t) = \zeta_{0k} \exp(\sigma_k t) & \text{for } t \le t_k^{sat}, \\ \zeta_k^{sat} \cdot \left[1 + \sigma_k (t - t_k^{sat})\right] & \text{for } t \ge t_k^{sat}, \end{cases} \tag{8.167}$$

where $t_k^{sat} = (1/\sigma_k) \ln(\zeta_k^{sat}/\zeta_0)$ is the time at which saturation occurs. Equation 8.167 can be written in the alternative form

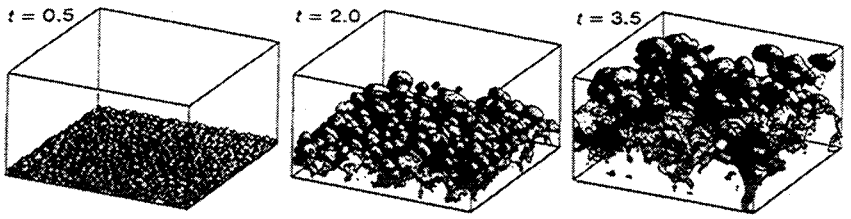

FIG. 8.28. Three-dimensional simulation of turbulent mixing due to the nonlinear evolution of a Rayleigh-Taylor unstable interface. The frames show the shape of the interface at three different times (in units of .....), as seen from the bubble side. After Youngs *et al.* (1994); reprinted with permission.

$$\zeta_k(t) = \begin{cases} \zeta_k^{\mathrm{lin}}(t) = \zeta_{0k} \exp(\sigma_k t) & \text{for } t \le t_k^{\mathrm{sat}}, \\ \zeta_k^{\mathrm{sat}} \cdot \left(1 + \ln \dfrac{\zeta_k^{\mathrm{lin}}(t)}{\zeta_k^{\mathrm{sat}}}\right) & \text{for } t \ge t_k^{\mathrm{sat}}, \end{cases} \tag{8.168}$$

which is widely used by ICF target designers.

Simulations have shown that this model is reasonably accurate for describing the instability up to some time after saturation and that it is well suited to the treatment of the instability of the outer surface of the ICF capsules. Improvements to the model have been proposed (Ofer *et al.* 1996; Town *et al.* 1996) to account for mode-coupling and for other more advanced features.

8.7.4 *Turbulent mixing*

The complexity of the later stages of the evolution of multimode RTI is shown by experiments and simulations. Examples are given by the last frame of Fig. 8.5 and by Fig. 8.28. Here we observe that, as time goes on, larger and larger structures appear and dominate the flow. Patterns become more and more complex and chaotic: we refer to this process as to turbulent mixing. While such features do not allow for any simple analytical treatment, important aspects are qualitatively described by dimensional arguments. These concern, in particular, the time evolution of the width of the turbulent mixing layer. It is defined by the quantities h_+ and h_- which measure the penetration of the bubbles into the heavier fluid and of the spikes into the lighter fluid, respectively.

If boundary conditions are not important, i.e. if the size of the whole system is larger than the largest flow structures, and memory of the initial conditions is lost, the flow is fully characterized by the acceleration a, the two densities ρ_1 and ρ_2, and time t. Dimensional analysis (see § 6.5) shows that there is only one dimensionless parameter, which may be chosen as the Atwood number A_t, and that all characteristic lengths such as bubble size $\lambda(t)$ and thickness $h(t)$ of the turbulent mixing layer will scale proportionally to at^2. This leads to the similarity

laws $\lambda(t) = f_\lambda(A_t)at^2$ and $h_\pm = f_{h_\pm}(A_t)at^2$ with factors f_λ and $f_{h_\pm}$ depending only on A_t. Such a self-similar description, first suggested by Youngs (1984) to explain the experimental results of Read (1984), accounts for the emergence of larger and larger structures in time and qualitatively agrees with large sets of experimental and simulation data. In particular, the experimental data on the width of the mixing layer, reviewed by Dimonte (2001), are reproduced by

$$h_\pm(t) = \alpha_\pm A_t a t^2, \tag{8.169}$$

Here, $\alpha_+ = 0.06$–0.07 for immiscible fluids and $\alpha_+ = 0.04$–0.044 for miscible fluids. The quantity α_- depends on A_t. Experimental results are fitted by by $\alpha_- = (1 + A_t)\alpha_+$ (Dimonte 1999), for $A_t \leq 0.9$. For $A_t \to 1$, instead, one expects $\alpha_- \to 0.5$. When the initial perturbation spectrum does not contain short wavelength modes, mixing develops after a well defined stage of linear evolution. In these cases, the width of the mixing layer is still well approximated by eq 8.169, but with time t replaced by $t - t_0$ where t_0 is a characteristic time marking the onset of turbulence (Atzeni and Guerrieri 1993).

For RMI, where there is no steady acceleration, one cannot form a quantity with the dimension of a length using dimensional quantities characterizing the flow. It then turns out that the thickness of the mixing layer depends on the initial conditions. It scales with time $\propto t^\theta$, with the exponent θ depending on the Atwood number. Theoretical treatments and experimental results on mixing by RMI can be found, e.g., in the papers by Dimonte (1999, 2000) and by Shvarts *et al.* (2001). KHI can also cause turbulent mixing. An interesting reference here is Brown and Roshko (1974).

8.8 RTI and target design

In this section, we apply the results obtained on RTI so far to ICF target design. RTI and related instabilities cause deformations of the shell's outer and inner surfaces with amplitudes ζ^{out} and ζ^{in}, respectively. Ignition of an ICF target requires that the fuel shell with thickness $\Delta R(t)$ maintains its integrity during implosion and a central hot spot with radius R_{h} is created at stagnation. Therefore, it is required that

$$\zeta^{\text{out}}(t) \ll \Delta R(t) \tag{8.170}$$

at any time t during implosion and

$$\zeta^{\text{in}}(t) \ll R_{\text{h}}, \tag{8.171}$$

at implosion stagnation.

We now use the results of linear and weakly nonlinear theory to estimate the constraints that inequalities 8.170 and 8.171 set to target and beam parameters. Following Lindl (1997), we consider ablative RTI, feed-through, and inner RTI. On the other hand, neglect cavity oscillations. Effects due to RMI and imprint

(see § 8.8.4) can be included by means of suitable initial conditions. We assume that initial perturbations have a wide spectrum and random phases, so that the amplitudes appearing in eqns 8.170 and 8.171 can be estimated as

$$\zeta \approx \sqrt{2}\zeta_{\rm rms} = \sqrt{\frac{1}{2\pi}\sum_l \zeta_l^2(2l+1)}, \tag{8.172}$$

where l is the spherical mode number.

8.8.1 *Perturbation growth at the ablation front*

According to linear theory, the amplitude reached at time t_0 by a perturbation of mode l at the ablation front is

$$\zeta_l^{\rm out} = \zeta_{l0}^{\rm out} G_l^{\rm out}. \tag{8.173}$$

Here, $\zeta_{l0}^{\rm out}$ is the initial amplitude, due to target imperfections and beam imprint,

$$G_l^{\rm out} = \exp\left(\int_0^{t_0} \sigma_l(t)dt\right) \tag{8.174}$$

is the growth factor, and σ_l is the linear growth rate of mode l. For the latter we use eqn 8.119, derived from linear theory of ablative RTI (see § 8.4). Setting $k = l/R$ to account for spherical geometry, we obtain

$$\sigma_l = \alpha_2\sqrt{\frac{al/R}{1+lL_{\rm min}/R}} - \beta_2\frac{l}{R}u_{\rm a}. \tag{8.175}$$

where $\alpha_2 \simeq 1$ and values of β_2 have been given in § 8.4.4. In order to compute the integral in eqn 8.174, we assume that the shell implodes at constant acceleration from $R = R_0$ to $R = R_0/2$, which takes a time $t_0 = \sqrt{R_0/a}$. We also assume that the largest value of $\zeta^{\rm out}/\Delta R$ is achieved just at $t = t_0$. Furthermore, we parametrize

$$L_{\rm min} = f_1\Delta R, \tag{8.176}$$

$$u_{\rm a} = f_2\Delta R(t_0)/t_0, \tag{8.177}$$

where f_1 and f_2 are numerical constants. The parameter f_1 depends on the shape of the density profile at the ablation front, while f_2 is related to the fraction of ablated mass and takes values of about 0.8 for indirect drive and 0.2 for direct drive. Inserting eqns 8.175–8.177 into eqn 8.174, and evaluating the integral by taking R and ΔR as constants, we obtain

$$G_l^{\rm out} \simeq \exp\left[\alpha_2\left(\frac{l}{1+l\dfrac{f_1}{2}\dfrac{\Delta R}{R}}\right)^{1/2} - \beta_2 f_2\frac{\Delta R}{R}l\right]. \tag{8.178}$$

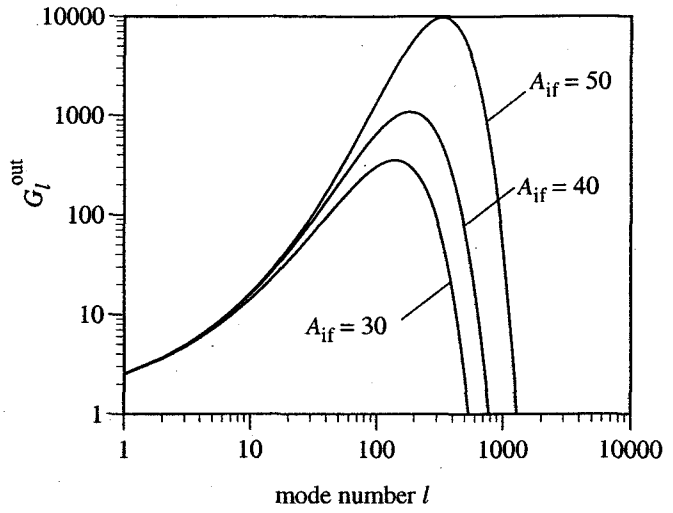

FIG. 8.29. Growth factor for outer surface perturbations versus the spherical mode number, for different values of the in-flight aspect ratio, and for fixed values of the parameters $f_1 = 0.1$ and $f_2\beta_2 = 0.8$.

Here, we interpret $R/\Delta R$ as a characteristic value of the in-flight-aspect-ratio. It follows immediately that modes with $l > l_{cut}$, with

$$l_{\rm cut} = \frac{R/\Delta R}{2f_1}\left(\sqrt{1+\frac{4f_1\alpha_2^2}{f_2^2\beta_2^2}\frac{R}{\Delta R}}-1\right) \tag{8.179}$$

are stable.

Equations 8.178 and 8.179 show that the growth factor $G_l^{\rm out}$ and the cut-off $l_{\rm cut}$ depend crucially on f_1, on the product $\beta_2 f_2$, and on the in-flight-aspect-ratio $R/\Delta R$. The behaviour of $G_l^{\rm out}$ as a function of the spherical mode number l is shown in Fig. 8.29. Here the growth factor is plotted for different values of the in-flight aspect ratio $A_{\rm if} = R/\Delta R$ and for fixed values of $f_1 = 0.1$ and $\beta_2 f_2 = 0.8$, typical of indirect-drive targets. The positive effect of a smaller in-flight aspect ratio is apparent. For $A_{\rm if} = 40$, which we can take as a reference value, the most unstable modes have l in the range 100–300 and corresponding growth factors of about 1000. Modes with $l < 10$ grow very little. For such modes, however, one has also to take into account the asymmetries caused by the secular growth of the deformations, discussed in § 3.2.1. Fig. 8.29

Figure 8.30 shows the perturbation spectrum obtained by the above model for an indirect-drive target with the same functional form of the perturbation spectrum as that assumed by the NIF target design (Marinak *et al.* 2001). Such a spectrum corresponds to an rms amplitude of about 12 nm. The calculation assumes $R/\Delta R = 40$, $f_1 = 0.1$, and $\beta_2 f_2 = 0.8$. We see that modes l = 100-400 Fig. 8.30

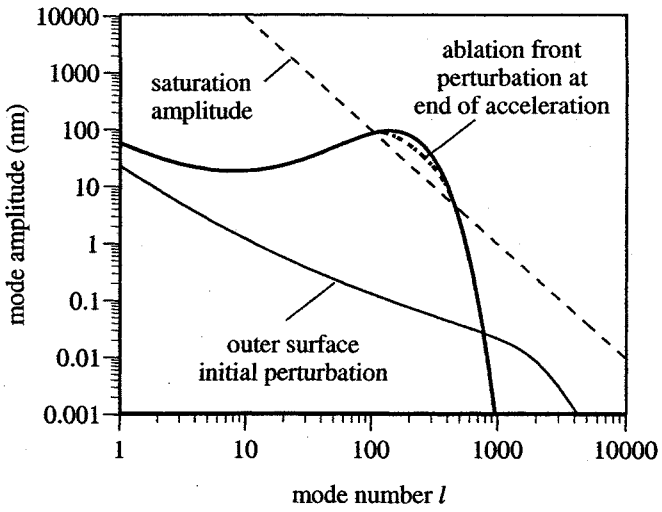

FIG. 8.30. Amplitude of RTI modes at ablation front, for parameters appropriate for indirect-drive targets and in-flight aspect ratio of 40. The final amplitudes (thick curves) are computed from linear theory (solid) and from the model for weakly nonlinear evolution (dot-dashed), in case the saturation amplitude (dashed line) is exceeded.

exceed the saturation threshold 8.165; in this case the growth is computed by eqn 8.168, and the corresponding result is shown by the dot-dashed curve. The root-mean-square amplitude of the perturbation turns out to be about 5 μm, sufficient for the safe implosion of a capsule with initial radius of 1 mm and in-flight shel thickness of about 15-20 μm

8.8.2 *Perturbation growth at the inner shell surface*

The inner surface of the shell becomes unstable when the imploding material starts to decelerate due to the pressure exerted by the inner hot gas. Seeds for such an instability are provided by both defects of the inner surface of the solid fuel with modal amplitudes $\zeta_{l00}^{\rm in}$ and feed-through from the ablation front (see § 8.2.9). The latter are caused by perturbations at the outer surface with spherical mode l and amplitude $\zeta_l^{\rm out}$ which are transmitted to the inner surface with amplitudes

$$\zeta_l^{\rm in-fed} = \zeta_l^{\rm out} G_l^{\rm fed} \simeq \zeta_l^{\rm out} \exp(-l\Delta R/R). \tag{8.180}$$

Assuming random phases, we estimate the effective initial amplitude of mode l as

$$\zeta_{l0}^{\rm in} \approx \left[(\zeta_{l00}^{\rm in})^2 + (\zeta_l^{\rm in-fed})^2\right]^{1/2}. \tag{8.181}$$

RTI will amplify such a perturbation according to

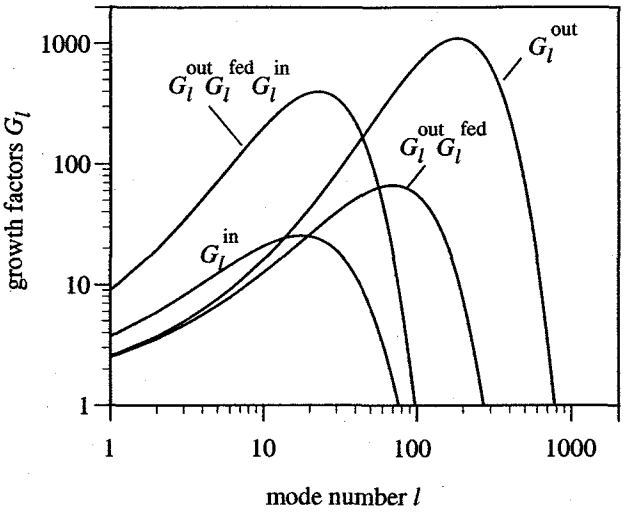

FIG. 8.31. Growth factors for RTI instability at both the outer and inner shell surfaces. Parameters are given in the main text.

$$\zeta_l^{\rm in} = \zeta_{l0}^{\rm in} G_l^{\rm in} = \zeta_{l0}^{\rm in} \exp \int_{t_{\rm dec}}^{t_{\rm dec}+\Delta t_{\rm dec}} \sigma_l^{\rm in}(t) dt, \qquad (8.182)$$

where $\sigma_l^{\rm in}$ is the growth rate 8.139 of the deceleration-phase instability and integration extends from the beginning of deceleration to the instant of ignition. To evaluate the integral we assume that the hot spot radius decreases from $R_{\rm dec}$ to $R_{\rm h}$ at constant deceleration, so that $a(\Delta t_{\rm dec})^2/2 = R_{\rm dec} - R_{\rm h}$. We then parametrize the decrease of the radius as $R_{\rm dec} - R_{\rm h} \approx f_3 R_{\rm h}$, the gradient scale-length as $L_{\rm in} = f_4 R_h$, and the ablation velocity as $u_{\rm ain} = f_5 R_{\rm h}/\Delta t_{\rm dec}$, where f_3, f_4, and f_5 are numerical constants. As representative values we may take $f_3 = 1$, $f_4 = 0.03$ and $\beta_{\rm in} f_5 \simeq 0.09$ (Lobatchev and Betti 2000, Atzeni and Temporal 2003). We then have

$$G_l^{\rm in} \approx \exp\left[\left(\frac{2f_3 l}{1+f_4 l}\right)^{1/2} - \beta_{\rm in} f_5 l\right] \approx \exp\left[\left(\frac{2l}{1+0.03l}\right)^{1/2} - 0.09\, l\right]. \qquad (8.183)$$

The resulting growth factors for feed-through and for the RTI at the inner layer are plotted in Fig. 8.31 for $A_{\rm if} = 40$. Fig. 8.31

The final amplitudes of the perturbations can now be computed from eqn 8.182. A representative example is shown in Fig. 8.32. The computations assume for the DT surface spectrum the same functional form as used by NIF designers (Marinak *et al.* 2001). A root-mean-square amplitude of 0.50 μm is assumed. Feed-through is computed assuming the outer surface perturbation of Fig. 8.30. It is found that the most dangerous modes have $l \approx 20$, higher modes being Fig. 8.32

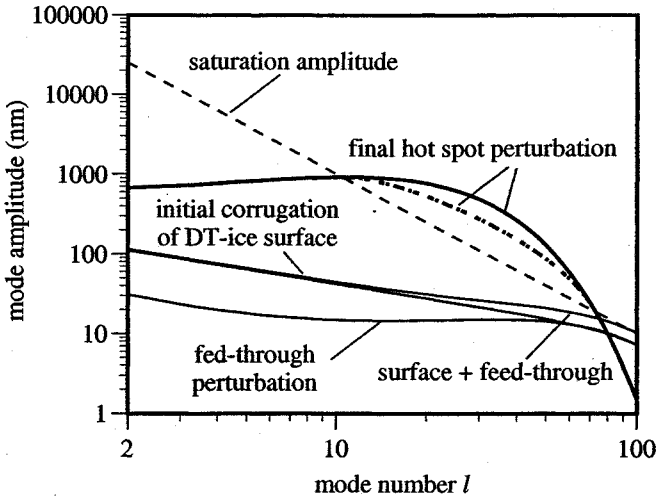

FIG. 8.32. Amplitude of RTI modes at stagnation, for the same capsule as in Figs 8.30 and 8.31. The figure shows the spectrum of the initial perturbation of the ice surface, of the contribution due to feed-through, and of the sum of the two, and (thick curves) of the final perturbation (solid: linear theory; dot-dashed: including correction for nonlinear evolution when saturation amplitudes are exceeded).

attenuated by feed-through and damped by the finite density gradient and ablation. The root-mean-square amplitude of the final perturbation is found to be about 5.6 μm. Since typically $R_h = 30$–40 μm, the computed perturbation should not hinder achievement of ignition.

8.8.3 *Target stability analysis by models and fluid codes*

Target design proceeds through several iterated steps, leading to a detailed point design of a capsule and including the analysis of the sensitivity to parameter changes. Concerning constraints set by instabilities, estimates are obtained by the model described in the previous subsections, but further analysis requires more accurate tools. The most advanced three-dimensional codes can now simulate the evolution of a wide spectrum of mode of a large sector of a capsule. A picture produced by the sophisticated 3D code HYDRA is shown in Fig. 8.33 (Marinak *et al.* 1996) and gives an idea of the level of detail achievable. Progress in computers, modeling, and programming allows even higher resolutions. A survey of state of the art simulations, as well as of the procedure followed to assess target sensitivity to instabilities, is given in a recent paper by Marinak *et al.* (2001). However, a single 3D run takes hundreds of hours on a massively parallel computer, and still it cannot resolve very short wavelengths. Parametric analysis requires tools easier to handle. Designers therefore use in combination

Fig. 8.33

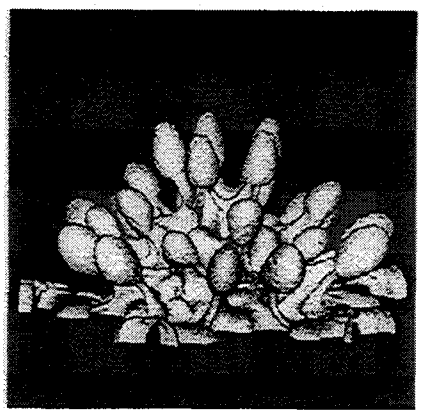

FIG. 8.33. 3D simulation of a capsule imploded by a thermal radiation pulse generated by the 10 beam laser NOVA. The picture shows the shape of the fuel-pusher interface at a time close to maximum compression. After Marinak *et al.* (1996), with permission.

1-D codes, 2D codes, and instability models.

Very accurate and yet reasonably fast 1-D computations allow to study basic capsule performance and to characterize the unperturbed flow, thus providing time-dependent values of such parameters as the in-flight aspect ratio, the characteristic scale-lengths, the acceleration, etc. required to compute the instability growth rates. The parameters they generate can also be fed into instability models, which solve numerically some simplified system of perturbed fluid equations to give the time evolution of the amplitude of the perturbation. Next, the effects of the perturbations on target performance can be approximately computed by 1-D simulations in which some shell layers are artificially mixed as to mimic the effect of RTI perturbations and mix.

2D simulations are particularly useful to compute self-consistently the time evolution of a perturbation with assigned spectrum, either single- or multi-mode. Of course, they have accuracy intermediate between the above rough models and 3D calculations. Notice, however, that present calculations of a whole target do not yet achieve the resolution required to study the highest-l unstable modes. This applies in particular to direct-drive, where ablative stabilization is effective at shorter wavelengths than in indirect-drive.

The design process eventually leads to specifications concerning target quality (surface roughness, homogeneity, etc.) and beam nonuniformities and imprint. Since targets must tolerate such imperfections with some margins, ignition experiments are designed to deliver 50-100% more energy to the fusion capsule than the minimum value computed by assuming perfectly spherical symmetry. We have seen in the previous subsection that a compromise has to be reached between the choice of the in-flight aspect ratio and surface as well as imprint

specifications. A smaller in-flight aspect ratio allows for rougher targets, but leads to lower energy gain and/or higher driver energy.

8.8.4 *Reducing target sensitivity to RTI*

Here, we mention a few options for relaxing instability constraints and widening the design parameter space. They are currently investigated, in particular, in order to the design of direct-drive targets.

A key issue for direct-drive is the so-called beam imprint, that is the target perturbation caused by the nonuniformity of the beam during the early stage of irradiation. Indeed laser beams are intrinsically noisy. Time-integrated homogeneous irradiation can be achieved by using *beam smoothing* techniques which mix statistically the incoherent beamlets of light of a broad bandwidth laser (Lehmberg and Hobenschain 1983; Skupsky *et al.* 1989). Experiments performed at different laboratories have indeed demonstrated that integrated implosion results, such as neutron production become approach the predictions of 1D simulations as beam uniformity is improved.

However, initial nonuniformities are unavoidable, even with the lasers having the largest bandwidth. Several methods have been proposed to reduce the effect of such *laser imprint*. Emery *et al.* (1991) proposed to coat the target with a low density foam, to reduce the perturbations stemming from the imperfect low intensity foot of the laser beam. In an alternative proposal, Obenschain *et al.* (2002) have demonstrated that the hydrodynamic instabilities seeded by the imprint are significantly reduced in foam targets coated with a thin high-Z layer. In this case, the low intensity laser foot is nearly completely absorbed by the high-Z layer. X-rays generated by this layer heat the low-Z plastic ablator and generate buffering plasma between the dense layer and the target to be accelerated. This layer isolates the target from the early laser nonuniformity. When the high power main pulse irradiates the the target, the high-Z layer expands and becomes transparent to the laser light. From this time on the target behaves just as the reference target studied in Chapter 3.

Other possible improvements concern means for reducing the growth of the RTI. According to eqn 8.178, RTI growth can be decreases with the ablation velocity. The latter, in turn increases as the shell density is decreases, i.e. its entropy is increased. On the other hand, we know that ignition and gain can only be achieved if the fuel is kept on a low adiabat. This leads to the concept of *adiabat shaping*: laser pulse and target are designed to keep the fuel on a low adiabat while increasing substantially the entropy of the ablator. It has been proposed to achieve adiabat shaping by irradiating the fuel shell by a shaped pulse preceded by a short high intensity picket (Metzler *et al.* 2002; Goncharov *et al.* 2003). This launches a strong shock through the ablator. However, as the laser intensity drops at the end of the picket, the shock strength decays and the shock does not negatively affect the compression of the inner fuel.

This has lead to the proposal increasing the density scale length at the ablation front has a beneficial effect on the linear growth rate. This can Some control

on such a length can be achieved by properly choosing the material composition of the ablator. A simpler, more effective way to achieve In particular, targets can be designed in such a way that X-rays generated in outer regions of the corona heat the unstable layer, but do not preheat the fuel (Obenschain *et al.* 2002).

8.9 Bibliographical note

There exists a broad literature on fluid instabilities relevant to ICF and in particular on Rayleigh-Taylor instability. In this section we list a few pedagogical publications of general interest, a number of review articles with direct relevance to ICF, and some articles presenting most advanced treatments of some specific topics.

The standard presentation of the linear theory of fluid instabilities is found in the textbook by Chandrasekhar (1961). There, Chapters X and XI deal with RTI and KHI in layered fluids, taking viscosity and surface tension into account; they are concluded by interesting bibliographical notes. Instabilities in stratified fluids are also discussed in the classical treatise on hydrodynamics by Lamb (1932): see § 231, § 232, § 267, and § 268.

An excellent review of RTI theory was presented by Kull (1991). Of particular interest in this article is the treatment of spherical shells and of nonlinear evolution of RTI bubbles. A historical note is also included.

Hoffman (1995) has published very clear and instructive lectures on important aspects of RTI theory with particular reference to ICF. A simple, but rather comprehensive tutorial was presented earlier by Sharp (1984). The book by Lindl (1997) on indirect-drive ICF also includes a long section on RTI and target design. Interesting reviews of instabilities in ICF have been written by Bodner (1991) and by Gamaly (1993). A book by Inogamov (1999) discusses fluid instabilities in the astrophysical context with emphasis on the theoretical modeling of the nonlinear stages of the RTI.

For a short review of experimental results on ablative RTI one can refer to a paper by Kilkenny *et al.* (1994). Important results obtained after publication of that paper have been quoted in § 8.4.5. An overview of self-consistent analytical theories of the ablative RTI is given by Betti *et al.* (1996).

It is also worth mentioning papers on aspects of RTI and RMI which have not been discussed in this chapter. The effect of self-generated magnetic fields on RTI have been discussed by Afanasev *et al.* (1978) and by Evans (1986). Cohesion effects in accelerated solids have been investigated experimentally by Dimonte *et al.* (1998). Impulsive acceleration, pulsation, accretion have been studied by Boris (1977), Rostoker (1977), Betti *et al.* (1993) and Book (1996), respectively. Experiments on mixing induced by time-dependent acceleration have been performed by Dimonte and Schneider (1996). The ablative RMI has been studied analytically by Goncharov (1999) and experimentally by Aglitskiy *et al.* (2002). Oscillations of fluid cavities and fluid shells have been analyzed in detail by Book and Bodner (1987) and by Kull (1991).

We now list papers with advanced, state of the art results on specific topics of relevance to ICF. Concerning ablative RTI, the standard reference for numerical eigenvalue solutions is Kull (1989), while the most advanced theoretical ones are summarized in the review of Betti *et al.* (1996). Ablative stabilization is also demonstrated by high resolution 2D numerical simulations; references here are the papers by Tabak *et al.* (1990), Gardner *et al.* (1991) and Mikaelian (1990). 3D simulations have become feasible since the early 1990s. Yabe *et al.* (1991) studied single-mode perturbations of a plane surface; Sagakami and Nishihara (1990) and Town and Bell (1991) simulated the instability at the inner surface of a stagnating shell; Dahlburg and Gardner *et al.* (1990) and Dahlburg *et al.* (1995) studied the instability at a laser driven ablation front. The most sophisticated target simulations have been reported by Marinak *et al.* (2001).

Overviews on mixing by both RTI and RMI have been published by Shvarts *et al.* (2000,2001) and by Dimonte (2000). Other interesting references on mixing are the papers by Alon *et al.* (1995), Dimonte (1999) and by Chen *et al.* (2000). The status of the research on RMI is summarized in a comprehensive review paper by Holmes *et al.* (1999), including many references on both theoretical and experimental results.

Laboratory astrophysics has been reviewed by Remington *et al.* (1999). They list many references to papers addressing instabilities in astrophysical objects.

References

Acheson, D. J. (1990). *Elementary Fluid Dynamics.* Clarendon, Oxford.

Afanasev, Yu. V., Gamalii, E. G., Lebo, I. G., and Rozanov, V. B. (1978). Hydrodynamic instability and spontaneous magnetic fields in a spherical laser plasma. *Soviet Physics JETP*, **47**, 271-5.

Aglitskiy, Y., Vekikovich, A. L., Karovik, M., Sevlin, V., Pawlet, C. J., Schmitt, A. J., Obenschain, S. P., Mostovich, A. N., Gardner, J. H., and Metzler, N. (2001). Direct observation of mass oscillations due to ablative Richtmyer-Meshkov instability in plastic targets. *Physical Review Letters*, **87**, 265001.

Alon, U., Hecht, J., Ofer, D., and Shvarts, D. (1995). Power laws and similarity of Rayleigh-Taylor and Richtmyer-Meshkov mixing fronts at all density ratios. *Physical Review Letters*, **74**, 534-7.

Amendt, P., Colvin, J. D., Ramshaw, J. D., Robey, H. F., and Landen, O. L. (2003). Modified Bell-Plesset effect with compressibility: application to double-shell ignition target designs. *Physics of Plasmas*, **10**, 820-8.

Atzeni, S., and Guerrieri, A. (1993). Evolution of multimode Rayleigh-Taylor instability towards self-similar turbulent mixing. *Europhysics Letters*, **22**, 603-9.

Atzeni, S., and Temporal, M. (2003). Mechanism of growth reduction of the ablative deceleration-phase Rayleigh-Taylor instability. *Physical Review E*, **67**, 057401 (4 pages).

Bell, G. I (1951). Taylor instability on cylinders and spheres in the small amplitude approximation. Technical Report LA-1321, Los Alamos Scientific Lab-

oratory.

Bernstein, I. B., and Book, D. L. (1983). Effect of compressibility on the Rayleigh-Taylor instability. *Physics of Fluids*, **26**, 453-8.

Betti, R., McCrory, R. L., and Verdon, C. P. (1993). Stability analysis of unsteady ablation fronts. *Physical Review Letters*, **71**, 3131-4.

Betti, R., Goncharov, V. N., McCrory, R. L., Sorotokin, P., and Verdon, C. P. (1996). Self-consistent stability analysis of ablation fronts in inertial confinement fusion. *Physics of Plasmas*, **3**, 2122-8.

Betti, R., Goncharov, V. N., McCrory, R. L., and Verdon, C. P. (1998). Growth rates of the ablative Rayleigh-Taylor instability in inertial confinement fusion. *Physics of Plasmas*, **5**, 1446-54.

Birkhoff, G. (1954). Note on Taylor instability. *Quarterly of Applied Mathematics* , **12**. 306-9.

Bodner, S. E. (1974). Rayleigh-Taylor instability and laser-pellet fusion. *Physical Review Letters*, **33**, 761-4.

Bodner, S. E (1981). Critical elements of high gain laser fusion. *J. Fusion Energy*, **1**, 221-40.

Bodner, S. E (1991). Symmetry and stability physics in laser fusion. In *Physics of Laser Plasma*, (ed. A. Rubenchik and S. Witkowski), pp. 247-70, North-Holland, Amsterdam.

Bodner, S. E., Colombant, D. G., Schmitt, A. J., and Klapisch (2000). High-gain direct-drive target design for laser fusion. *Physics of Plasmas*, **7**, 2298-301.

Book, D. L. (1996). Suppression of the Rayleigh-Taylor instability through accretion. *Physics of Plasmas*, **3**, 354-9.

Book, D. L., and Bodner, S. E. (1987). Variation of the amplitude of perturbations of the inner surface of an imploding shell during the coasting phase. *Physics of Fluids*, **30**, 367-76.

Boris, J. P. Dynamic stabilization of the imploding shell Rayleigh-Taylor instability. *Comments on Plasma Physics and Controlled Fusion*, **3**, 1-13.

Brenner, M. P., Hingenfeldt, S., and Lohse, D. (2002). Single-bubble sonoluminescence. *Review of Modern Physics*, **74**, 425-84.

Brown, G. L., and Roshko, A. (1974). On the density effect and large structure in turbulent mixing layers. *Journal of Fluid Mechanichs*, **64**, 775-816.

Budil, K. S., Remington, B. A., Peyser, T. A., Mikaelian, K. O., Miller, P. L., Woolsey, N. C., Wood-Vasey, W. M., and Rubenchik, A. M. (1996). Experimental comparison of classical versus ablative Rayleigh-Taylor instability. *Physical Review Letters*, **76**, 4536-9.

Budil, K. S., Lasinski, B., Edwards, M. J., Wan, A. S., Remington, B. A., Weber, S. V., Glendinning, S. G., Suter, L., and Stry, P. E. (2001). The ablation-front Rayeligh-Taylor dispersion curve in indirect drive. *Physics of Plasmas*, **8**, 2344-8.

Chandrasekhar, S. A (1961). *Hydrodynamic and Hydromagnetic Stability*. Oxford.

Chen, Baolian, Glimm, J., Sharp, D. H. (2000). Density dependence of Rayleigh-Taylor and Richtmyer-Meshkov mixing fronts. *Phys. Lett. A* **268**, 366-74.

A. J. Cole, J. D. Kilkenny, P. T. Rumsby, R. G. Evans, C. J. Hooker, and M. H. Key (1982). Measurement of Rayleigh-Taylor instability in a laser-accelerated target. Nature, **299**, 329-30.

Colombant, D. G. , Bodner S. E., Schmitt A. J., Klapisch M., Gardner J. H., Aglitskiy Y., Deniz A. V., Obenschain S. P., Pawley C. J., Serlin V., and Weaver J. L. (2000). Effects of radiation on direct-drive laser fusion targets. *Physics of Plasmas*, **7**, 2046-2054.

Dahlburg, J. P., and Gardner, J. H. (1990). Ablative Rayleigh-Taylor instability in three dimensions. *Physical Review A*, **41**, 5695-8.

Dahlburg, J. P., Fyfe, D. E., Gardner, J. H., Haan, S. W., Bodner, S. E., and Doolen, G. D. (1995). Three-dimensional multimode simulations of the ablative Rayleigh-Taylor instability. *Physics of Plasmas*, **2**, 2453-9.

Dimonte, G. and Schneider, M. (1996). Turbulent Rayleigh-Taylor instability experiments with variable acceleration. *Physical Review E*, **54** 3740-3.

Dimonte, G., Gore, R., and Schneider, M. (1998). Rayleigh-Taylor instability in elastic-plastic materials. *Physical Review Letters*, **80**, 1212-5.

Dimonte, G. (1999). Nonlinear evolution of the Rayleigh-Taylor and Richmeyer-Meshkov instabilities. *Physics of Plasmas*, **6**, 2009-15.

Dimonte, G. (2000). Spanwise homogeneous buoyancy-drag model for Rayleigh-Taylor mixing and experimental evaluation. *Physics of Plasmas*, **6**, 2009-15.

Emery, M. H., Gardner, J. H., Lehmberg, R. H., and Obenschain, S. P. (1991). Hydrodynamic target response to an induced spatial incoherence-smoothed laser-beam. *Physics of Fluids B*, **3**, 2640-51.

Evans, R. G., Bennett, A. J., and Pert, G. J. (1982) Rayleigh-Taylor instabilities in laser-accelerated targets. *Physical Review Letters*, **49**, 1639-42.

Evans, R. G. (1986). The influence of self-generated magnetic fields on the Rayleigh-Taylor instability. *Plasma Physics and Controlled Fusion*, **28**, 1021-4.

Gamaly, E. G. (1993). Hydrodynamic instability of target implosion in ICF. In *Nuclear Fusion by Inertial Confinement: a comprehensive treatise* (ed. G. Velarde, Y. Ronen, J. M. Martinez-Val), pp. 321-49. CRC Press, Baton Roca.

Gardner, J. H., Bodner, S. E., Dahlburg, J. P. (1991). Numerical simulation of ablative Rayleigh-Taylor instability. *Physics of Fluids B* 3, 1070-4.

Glendinning, S. G., Dixit, S. N., Hammel, B. A., Kalantar, D. H., Key, M. H., Kilkenny, J. D., Knauer, J. P., Pennington, D. M., Remington, B. A., Wallace, R. J., and Weber, S. V. (1997). Measurement of a dispersion curve for linear-regime Rayleigh-Taylor growth rates in laser-driven planar targets. *Physical Review Letters*, **78**, 3318-21.

Goncharov, V. N. (1999). Theory of the ablative Richtmyer-Meshkov instability. *Physical Review Letters*, **82**, 2091-4.

Goncharov, V. N., Knauer, J. P., McKenty, P. W., Radha, P. B., Sangster, T. C., Skupsky, S., Betti, R., McCrory, R. L., and Meyerhofer, D. D. (2003).

Improved performance of directy-drive inert *Physics of Plasmas*, **10**, 1906-18.

Grove, J. W., Holmes, R., Sharp, D. H., Yang, Y., Zhang, Q. (1993). Quantitative theory of the Richtmyer-Meshkov instability. *Physical Review Letters*, **71**, 3473-6.

Grun, J., Emery, M. H., Kacenjar, S., Opal, C. B., McLean, E. A., Obenschain, S. P., Ripin, B. H., and Schmitt, A. (1984). Observation of the Rayleigh-Taylor instability in ablatively accelerated foils. *Physical Review Letters*, **53**, 1352-5.

Haan, S. W. (1989). Onset of nonlinear saturation for Rayleigh-Taylor growth in the presence of a full spectrum of modes. *Physical Review A*, **39**, 5812-25.

Haan, S. W. (1991). Weakly nonlinear hydrodynamic instabilities in inertial fusion. *Physics of Fluids B*, **3**, 2349-55.

Hattori, F., Takabe, H., and Mima, K. (1986). Rayleigh-Taylor instability in a spherically stagnating system. *Physics of Fluids*, **29**, 1719-24.

Hecht, J., Ofer, D., Alon, U., Shvarts, D., Orszag, S. A., and McCrory, R. L. (1995). Three-dimensional simulation of the nonlinear stage of the Rayleigh-Taylor instability. *Laser and Particle Beams*, **13**, 423-40.

Hoffman, N. M (1995). Hydrodynamic instabilities in inertial confinement fusion, (ed. M. B. Hooper). In *Laser Plasma Interactions 5: Inertial Confinement Fusion*, pp. 105-37. Institute of Physics Publishing, Bristol.

Holmes, R. L., Dimonte, G., Fryxell, B., Gittings, M. L., Grove, J. W., Schneider, M., Sharp, D. H., Velikovich, A. L., Weaver, R. P., and Zhang, Q. (1999). Richtmyer-Meshkov instability growth: experiment, simulation and theory. *Journal of Fluid Mechanics*, **389**, 55-79.

Inogamov, N. A. (1999). The role of Rayleigh-Taylor and Richtmyer-Meshkov instabilities in astrophysics: An introduction. *Astrophysics and Space Physics Reviews* **10**, 1-335.

Jacobs, J. W., and Catton, I. (1988). Three-dimensional Rayleigh-Taylor instability Part 1. Weakly nonlinear theory. *Journal of Fluid Mechanics*, **187**, 329-52.

Kilkenny, J. D., Glendinning, S. G., Haan, S. W., Hammel, B. A., Lindl, J. D., Munro, D., Remington, B. A., Weber, S. V., Knauer, J. P., and Verdon, C. P. (1994). A review of the ablative stabilization of the Rayleigh-Taylor instability in regimes relevant to inertial confinement fusion. *Physics of Plasmas*, **1**, 1379-89.

Kull, H. J. (1983). Bubble motion in the Rayleigh-Taylor instability. *Physical Review Letters*, **51**, 1437-40.

Kull, H. J. (1989). Incompressible description of Rayleigh-Taylor instabilities in laser-ablated plasmas. *Physics of Fluids B*, **1**, 170-82.

Kull, H. J. (1991). Theory of the Rayleigh-Taylor instability. *Physics Reports*, **206**, 197-325.

Kull, H. J., and Anisimov, S. I. (1986). Ablative stabilization in the incompressible Rayleigh-Taylor instability. *Physics of Fluids*, **29**, 2067-75, 1986.

Lamb, H. (1932). *Hydrodynamics*, 6th ed. Cambridge.

Landau, L. D., and Lifshitz, E. M. (1987). *Fluid Mechanics*, 2nd ed. Butterworth-Heinemann, Oxford.

Layzer, D. (1955). On the instability of superposed fluids in a gravitational field. *Astrophysical Journal*, **122**, 1-12.

Le Levier, R, Lasher, G. J., and Bjorklund, F. (1955) Effect of a density gradient on Taylor instability. Technical Report UCRL-4459, LLNL, Livermore.

Lehmberg, R. H., and Obenschain, S. P. (1983). Use of induced spatial incoherence for uniform illumination of laser fusion targets. *Optics Communications*, **46**, 27-31.

Lewis, J. D. (1950). The instability of liquid surfaces when accelerated in a direction perpendicular to their planes. II. *Proceedings of the Royal Society (London)*, **A202**, 81-96.

Lindl, J. D., and Mead, W. C. (1975). Two-dimensional simulation of fluid instability in laser-fusion pellets. *Physical Review Letters*, **34**, 1273-6.

Lindl, J. D. (1997). *Inertial confinement fusion: the quest for ignition and high gain using indirect drive*. Springer and AIP, New York.

Lohse, D. (2003). Bubble Puzzles. *Physics Today*, February, pp. 36-41.

Lobatchev, V., Betti, R. (2000). Ablative stabilization of the deceleration phase Rayleigh-Taylor instability. *Physical Review Letters*, **85**, 4522-5.

Marinak, M. M., Tipton, R. E., Landen, O. L., Murphy, T. J., Amendt, P., Haan, S. W., Hatchett, S. P., Keane, C. J., McEachern, R., and Wallace, R. (1996). Three-dimensional simulations of Nova high growth factor capsule implosion experiments. *Physics od Plasmas*, **3**, 2070-6.

Marinak, M. M., Kerbel, G.D., Gentile, N. A., Jones, O., Munro, D., Pollaine, S., Dittrich, T. R., and Haan, S. (2001). Three-dimensional simulations of National Ignition Facility targets. *Physics od Plasmas*, **8**, 2275-80.

McKenty, P. W., Goncharov, V. N., Town, R. P. J., S. Skupsky, R. P. J., Betti, R., and McCrory, R. L. (2001) Analysis of a direct-drive ignition capsule designed for the National Ignition Facility *Physics od Plasmas*, **8**, 2315-22.

McCrory,R.L., Montierth, L., Morse, R. L., and Verdon, C. P. (1981) Nonlinear evolution of ablation-driven Rayleigh-Taylor instability. *Physical Review Letters*, **46**, 336-9.

Menikoff, R., Mjolsness, R.C., Sharp, D. H., and Zemach, C. (1977). Unstable normal modes for Rayleigh-Taylor instability in viscous fluids. *Physics of Fluids*, **20**, 2000-4.

Meshkov (1969). Instability of the interface of two gases accelerated by a shock wave. *Izv. AN SSSR. Mekhanika Zhidkosti i Gaza*, **4**, 151-157.

Meyer, K. A., and Blewett, P. J. (1972). Numerical investigation of the stability of a shockaccelerated interface between two fluids. *Physics of Fluids*, **15**, 753-759.

Metzler, N., Velikovich, L., Schmitt, A. J., and Gardner, J. H. (2002). Laser imprint reduction with a short shaping laser pulse incident upon a foam-plastic target. *Physics of Plasmas*, **9**, 5050-8.

Mikaelian, K. O. (1990). LASNEX simulations of the classical and laser-driven Rayleigh-Taylor instability. *Physical Review A*, **42**, 4944-51.

Munro, D. H. (1988). Analytic solutions for Rayleigh-Taylor growth rates in smooth density gradients. *Physical Review A*, **38**, 1433-45.

Nakai, S., Yamanaka, T., Izawa, Y., Kato, Y., Nishihara, K., Nakatsuka, M., Sasaki, T., Takabe, H., *et al.* (1995). Present status and future prospects of laser fusion research at ILE, Osaka. In *Plasma Physics and Controlled Fusion Research 1994, Fifteen International Conference proceedings, Seville, Spain, 28 September - 1 October 1994*, vol. 3, pp. 3-12. IAEA, Vienna.

Obenschain, S. P., Colombant, D. G., Karasik, M., Pawley, C. J., Serlin, V., Schmitt, A. J., Weaver, J. L., Gardner, J. H., Phillips, L., Aglitskiy, Y., Chan, Y., Dahlburg, J. P., and Klapisch, M. (2002). Effects of thin high-Z layers on the hydrodynamics of laser-accelerated plastic targets. *Physics of Plasmas*, **9**, 2234-43.

Ofer, D., Alon, U., Shvarts, D., McCrory, R. L., and Verdon, C. P. (1996). Modal model for the nonlinear multimode Rayleigh-Taylor instability. *Physics of Plasmas*, **3**, 3073-90.

Oron, D., Alon, U., and Shvarts, D. (1998). Scaling lasws of the Rayleigh-Taylor ablation front mixing zone evolution in inertial confinement fusion *Physics of Plasmas*, **5**, 1467-76.

Piriz, A. R. (2001a). Hydrodynamic instability of ablation fronts in inertial confinement fusion. *Physics of Plasmas*, **8**, 997-1002.

Piriz, A. R. (2001b).Compressibility effects on the RayleighTaylor instability of an ablation front. *Physics of Plasmas*, **8**, 5268-76.

Plesset, M. S. (1954). On the stability of fluid flows with spherical symmetry. *Journal of Applied Physics*, **25**, 96-98.

Read, K. L. (1984). Experimental investigation of turbulent mixing by Rayleigh-Taylor instability. *Physica*, **12**, 45-52.

Remington, B. A., Haan, S. W., Glendinning, S. G., Kilkenny, J. D., Munro, D. H., and Wallace, R. J. (1991). Large growth Rayleigh-Taylor experiments using shaped laser pulses. *Physical Review Letters*, **67**, 3259-62.

Remington, B. A., Arnett, D. A., Drake, R. P., and Takabe, H. (1999). Modeling astrophysical phenomena in the laboratory with intense lasers. *Science*, **284**, 1488-93.

Richtmyer, R. D (1960). Taylor instability in shock acceleration of compressible fluids. *Comm. Pure Appl. Mathematics*, **13**, 297-319.

Rostoker, N, and Tahsiri, H. (1977). Rayleigh-Taylor instability of impulsively accelerated shells. *Comments on Plasma Physics and Controlled Fusion*, **3**, 39-45.

Sakagami. H., and Nishihara, K (1990). Three-dimensional Rayleigh-Taylor instability of spherical systems. *Physical Review Letters*, **65**, 432-5.

Sanz, J. (1994) Self-consistent analytical model of the Rayleigh-Taylor instability in inertial confinement fusion. *Physical Review Letters*, **73**, 2700-3.

Sanz, J., Ramirez, J., Ramis, R., Betti, R., and Town, R. P. J. (2002). Nonlinear

Rayleigh-Taylor instability in the deceleration phase of spherical implosion experiments.

theory of the ablative Rayleigh-Taylor instability. *Physical Review Letters*, **89**, 195002.

Sharp, D. H. (1984). An overview of Rayleigh-Taylor instability. *Physica*, **12D**, 3-18.

Shvarts, D., Oron, D., Kartoon, D. Rikanati, A. Sadot, O. , Srebro, Y., Yevdab, Y., Ofer, D., Levin, A., Sarid, E., Ben-Dor, G., Erez, L., Erez, G., Yosef-Hai, A., Alon, U., and Arazi, L. (2000). Scaling laws of nonlinear Rayleigh-Taylor and Richtmyer-Meshkov instabilities in two and three dimensions. In *Inertial fusion sciences and applications 99*, (eds. C. Labaune, W. J. Hogan, and K. A. Tanaka), pp. 197-204. Elsevier, Paris.

Shvarts, D., Sadot, O., Oron, D., Rikanati, A., and Alon, U. (2001). Shock-induced instability of interfaces. In *Handbook of shock waves*, vol. 2, (eds. G. Ben-Dor, O. Igra, and T. Elperrin), pp. 489-543. Academic, New York.

Skupski, S., Short, R. W., Kessler, T., Craxton, R. S., Letzring, S., and Soures, J. M. (1989). *Journal of Applied Physics*, **66**, 3456-62.

Smalyuk, V. A., Delettrez, J. A., Goncharov, V. N., Marshall, F. J., Meyerhofer, D. D., Regan, S. P., Sangster, T. C., Town, R. P. J., and Yaakobi, B. (2002). *Physics of Plasmas*, **9**, 2738-44.

Tabak, M., Munro, D. H., and Lindl, J. D. (1990). Hydrodynamic stability and the direct drive approach to laser fusion. *Physics of Fluids B*, **2**, 1007-14.

Takabe, H., Mima, K. , Montierth, L., and Morse, R. L. (1985). Self-consistent growth rate of the Rayleigh-Taylor instability in an ablatively accelerating plasma. *Physics of Fluids*, **28**, 3676-82.

Taylor, G. (1950). The instability of liquid surfaces when accelerated in a direction perpendicular to their planes. I. *Proceedings of the Royal Society (London)*, **A201**, 192-6.

Town, R. P. J., and Bell, A. R. (1991). Three-dimensional simulations of the implosion of inertial confinement fusion targets. *Physical Review Letters*, **67**, 1863-6.

Town, R. P. J., Findlay, J. D., and Bell, A. R. (1996). Multimode modelling of the Rayleigh-Taylor instability. *Laser and Particle Beams*, **14**, 237-51.

Yabe, T., Hoshino, H., and Tsuchiya. T. (1991). Two- and three-dimensional behavior of Rayleigh-Taylor and Kelvin-Helmholtz instabilities. *Physical Review A*, **44**, 2756-8.

Youngs, D. L. (1984). Numerical simulation of turbulent mixing by Rayleigh-Taylor instability. *Physica*, **12 D**, 32-44.

Youngs, D. L. (1994. Numerical simulation of mixing by Rayleigh-Taylor and Richtmyer-Meshkov instabilities. *Laser and Particle Beams*, **12**, 725-50.

Zhang, Q. (1998). An analytical solution of Layzer-type approach to unstable interfacial fluid mixing. *Physical Review Letters*, **81**, 3391-4.

← Spitzer, L. J. (1962). Physics of fully ionized plasmas. 2nd edn. Interscience, New York.